Modelling and prediction of cavitation erosion in GDi injectors operated with E100 fuel

Eduardo Gomez Santos[a,b], Junmei Shi[a,*], Ramesh Venkatasubramanian[a], Guy Hoffmann[a], Manolis Gavaises[b], Wolfgang Bauer[c]

[a] *Delphi Technologies, Avenue de Luxembourg, 4940 Bascharage, Luxembourg*
[b] *City, University of London, Northampton Square, London EC1V 0HB, UK*
[c] *ANSYS Germany GmbH, Staudenfeldweg 20, 83624 Otterfing, Germany*

Abstract

Ethanol (E100) can be utilised in spark ignition engines for passenger car vehicles. This brings a challenge to the durability of the fuel injection system components since its use can result in corrosion, further enhanced by cavitation-induced erosion. This work reports computational fluid dynamics (CFD) predictions for both the flow development and the locations prone to cavitation erosion in multi-hole gasoline direct injection (GDi) injectors operated with E100. The compressible form of the Navier-Stokes equations is solved numerically considering the motion of the injector's needle valve. Thermodynamic and mechanical equilibrium is assumed between the liquid, vapour and non-condensable gas; E100 liquid and vapour are considered as a barotropic fluids where the corresponding variation in density with pressure and the speed of sound are estimated via a relevant equation of state; an

*Corresponding author
Email address: junmei.shi@delphi.com (Junmei Shi)

additional transport equation is solved for simulating the non-condensable air entrainment into the injector during the dwell time between successive injections. Turbulence is modelled using both large eddy simulation (LES) and Unsteady Reynolds-averaged Navier-Stokes (URANS) considering a sector and the full nozzle geometry, respectively. Various cavitation erosion indices reported in the literature are evaluated against new durability tests of surface erosion damage obtained after 400M injection cycles. The relevant nozzle wall erosion images are found to correlate well with the accumulated erosive power predicted from the computational model.

Keywords: Cavitation, Erosion, E100 fuel, Gasoline Direct injection, LES, URANS,

1. Introduction

The increased use of bio-ethanol as a renewable fuel in internal combustion engines can to significantly reduce their net CO_2 emissions. For this reason, bio-ethanol blended fuels have gained increasing interest in the transportation sector in order to meet the emission legislation limits imposed worldwide. In Europe, E10 (10% ethanol-gasoline fuel mix) is the standard fuel mix for petrol engines, while a further increase of the ethanol percentage is under discussion by the relevant bodies. In Brazil there is even a market demand for developing engines able to run with E100 fuels [1].

GDi engines are moving towards using higher injection pressures in the range of 350 *bar* to more than 500 *bar*. Under such conditions, formation of

Nomenclature

α_{air}	air volume fraction [-]	D	injection hole diameter [m]
α_{liq}	liquid fuel volume fraction [-]	E	potential energy of a spherical bubble $[J]$
α_{vap}	vapour fuel volume fraction [-]	e	potential energy of a cavity per unit volume $[J/m^3]$
$\boldsymbol{v}$	velocity field $[m/s]$	p	pressure $[Pa]$
λ_g	Taylor length scale [m]	R	bubble radius $[m]$
μ	molecular viscosity $[Pa\ s]$	Re	Reynolds number [-]
μ_t	turbulent viscosity $[Pa\ s]$	y^+	non-dimensional wall distance [-]
ρ	density $[kg/m^3]$		

cavitation and its impact on the spray behaviour has been reported [2].

Due to their production process, ethanol fuels can contain water and trace contaminants such as inorganic chlorides and sulphates, which can cause corrosion damage and enhance deposit formation [3] on the hydraulic components of the fuel injection system; thus, causing durability issues [4]. It is generally understood that the corrosion damage can be enhanced by cavitation erosion [5, 6]; this fact, together with the observation of damage in areas where cavitation is developing, led to the hypothesis that the well-known ethanol induced corrosion of hydraulic components is enhanced by the presence of cavitation.

Cavitation can be described as the process of vapour formation from pre-

existing nuclei when the local pressure falls below the vapour pressure of the flowing liquid [7, 8]. When pressure recovers to values above the liquid's vapour pressure, vapour condenses back into liquid creating strong pressure waves, which can damage the nearby walls [9]. Remarkably, the cavitation collapse process can result in light emission and temperatures in some cases of the order of $9000\,K$ very localised in time and space [10, 11]. Given the severity of cavitation collapse, plastic deformation and/or erosion of metallic surfaces causing performance drift and/or failure in multiple industrial scenarios such as in ship propellers [12], and high pressure fuel injection systems (including pumps [13, 14] and injectors [15]) have been reported.

Additionally, liquids usually contain dissolved gases that are released by pressure drop or cavitation [16]; therefore, cavitation bubbles typically contain gases which greatly affects the collapse dynamics and severity [17]. Indeed, it was shown in [18] and numerically reproduced in [19] that the initial energy of a bubble splits into the rebound energy and the energy carried away by the emitted shock wave. Free gas content (given by the gas partial pressure inside the vapour bubble) has a damping effect that weakens the pressure wave and enhances the bubble rebound. As explained in [20, 21] common cavitation bubble collapse experiments use laser or spark-induced bubbles that behave like hydrodynamic cavitation bubbles; when the maximum radius is reached, the bubble dynamics are no longer influenced by the initial hot plasma forming inside the bubble.

The experiments of [22] with transparent glass GDi nozzles using differ-

ent fuels relevant to spark ignition engines (including pure gasoline, E10 and E100 fuels), with injection temperatures ranging from $20\,C^o$ to $90\,C^o$ and back pressures ranging from $0.5\,bar$ to $1\,bar$ show that cavitation occurs at all the conditions tested. Further transparent nozzle experiments also confirm the presence of cavitation in GDi injectors [23, 24, 25]. Cavitation inside fuel injectors presents several distinct morphologies. Sharp throttle corners usually induce the so-called cloud cavitation which forms during the growth of cavitation bubbles at the entry of the injection hole [26]; this is followed by shedding of the formed vapour clouds due to flow instability (see selectively [27, 28, 29]). Moreover, the swirling flow conditions prevailing due to the complex recirculation of the flow inside the injector's sac volume, also induce cavitation at the core of the formed vortices (so-called string cavitation, see selectively [30, 31, 32, 33]). Notwithstanding, during the dynamic movement of the injector needle valve, needle seat cavitation has been observed [32] and substantial cavitation in the nozzle's sac volume at the end of the injection has been numerically predicted [34, 35, 29]; distinguishing vapour from ingested air is not straightforward from experimental observations.

In terms of modelling the cavitating flow in fuel injection applications both Eulerian and Eulerian-Lagrangian approaches have been reported, including full thermodynamic closure and friction-induced heating effects in high pressure fuel injection systems [36, 37, 38, 39, 40]. In the most general formulation of Eulerian heterogeneous multi-fluid models, each phase has its own pressure, velocity and temperature; source terms in the conserva-

tion equations determine the momentum mass and energy exchange between the phases [41]. These models unavoidably present increased modelling and computational requirements. Under the assumption of all phases sharing the same pressure and isothermal flow [42], in a throttle flow resembling a Diesel injector, the slip velocity between the phases was found to be less than 15% of the liquid bulk velocity and only in very localized regions. As the inertia of the vapour/air phases is small compared to that of the bulk liquid [43], mechanical and thermal equilibrium can be assumed, leading to a single velocity field for all co-existing phases. These models are known as homogeneous mixture or single-fluid models and resemble the traditional single-phase Navier-Stokes equations complemented by an additional transport equation expressing the mass conservation of non-condensable gas; moreover, a source term can be used to model the mass transfer between liquid and vapour, such as the widely used models of [8, 44, 45]. These models contain empirically calibrated constants that determine the mass transfer rate and have been shown to be equivalent if the constants are chosen appropriately [46]; typically, low values of the calibration constants are selected, which may results in non-physical negative pressures [47]. Moreover, this also results in a severe over-prediction of the collapse time of cavitation bubbles [47, 48, 49]. The error can be reduced by model calibration to match the critical cavitation point measurement (CCP) for different throttle configurations as it is reported in [50]; still this empirical approach is not efficient and reliable considering that all the model parameters need to be calibrated simultaneously. The ad-hoc

increase of the calibration coefficients corrects these issues and is in line with the experimental evidence of [51], where the pressure inside a cavitation cavity for a flow of water through a throttle was measured. For water, there is a close agreement between the measured pressure and the vapour pressure, which indicates that the cavity is almost filled with saturated vapour of water and that the vapour and liquid mixture is in thermodynamic equilibrium. This motivates the use of thermodynamic equilibrium models in which the mixture's vapour volume fraction is obtained from the mixture density and the saturation densities of liquid and vapour at the equilibrium temperature, without the need to solve for any additional transport equation [52, 53]. Thermodynamic equilibrium models can be further simplified by not solving the energy equation and considering the density to be exclusively a function of pressure (barotropic models). Simulation results for the collapse of a bubble cluster show negligible impact of the barotropic assumption on the collapse characteristics of bubble clusters [54]; similarly, simulation results for a cavitating mixing layer show negligible heating effects [55]. Finally, barotropic models are essentially equivalent to finite rate mass transfer models with increased mass transfer coefficients [56, 47].

Resolution of turbulent structures is key in describing vortex cavitation, cavitation shedding and flow unsteadiness. URANS models may fail to predict simple shedding in throttle flows, although by modifying and reducing the eddy viscosity in cavitating regions the unsteadiness can be reproduced in some situations [57, 58]. Despite this, in [59, 47] URANS models failed to

predict incipient cavitation when the pressure difference driving the flow was low. This shows that URANS models are situational and lack universality in the prediction of cavitation. On the other hand, scale resolving simulations (such as LES and DES) can predict the formation of cavitation in the case of incipient cavitation for both barotropic and finite rate mass transfer models [47]; see also the first published LES simulations in fuel injectors [60]. This type of modelling can also predict areas prone to cavitation erosion in fuel injectors, using both finite rate mass transfer [15] and barotropic models [34]; they have been thoroughly validated up to the accuracy of the measuring devices in the case of finite rate mass transfer models [61].

Identifying the parameters that are most suitable for predicting cavitation erosion in a CFD simulation is still an open research question. Some studies rely on resolving the mechanical loads of cavitation collapses reaching the walls and recording the maximum pressure [15, 34]. The drawback of this method is that the value of the recorded pressure peaks can be mesh and time resolution dependent [52, 49]. In addition in fuel injectors due to the moving needle valve, the sac volume pressure presents variations of the order of the injection pressure, which can obscure pressure peaks arising during the different injection phases [62]. Other investigations have successfully explored methods based on the potential energy available in cavities [63, 49, 64] or pressure time derivatives [65, 14, 13]. Finally, some works attempt to include also the material properties of the eroded metal such as that mean depth penetration rate (MDPR) [8, 66] or the accumulated impact

energy of [67]. The MDPR suggests treatment of the material response to repeated loading due to cavitation, while the accumulated impact energy sums the pressure waves reaching the walls with an intensity above the yield strength of the material. This last parameter therefore requires accurate resolution of the pressure field that only compressible LES formulations can provide. Nevertheless, a simulation tool suitable for obtaining cavitation erosion diagnostic at industrially affordable computational time scales while being able to support and interpret the durability tests, is very much desirable in the relevant industries.

Injector durability tests are expensive since they require many operation cycles and they do not reveal the detailed flow processes leading to erosion; still, they can be used to validate relevant simulation models, which in turn, are helpful to understand the underlying physics.

This work focuses on modelling the turbulent cavitating flow inside multi-hole GDi injectors operated with E100. Durability tests employing 400 million injection cycles have been performed at Delphi Technologies for some prototype nozzles; surface damage in the sac volume walls and spray hole inlet, where cavitation occurrence is expected have been observed; erosion damage was not observed when using other common fuels with lower ethanol mix fuels, such as the commonly used E10, at the specific injector and operating conditions.

Simulations of GDi nozzle flow have been reported for the so-called “Spray G” injector of the Engine Combustion Network (ECN) with moving needle

valve [68, 69, 70]. However, to the best of the author's knowledge, this is the first CFD investigation of cavitation erosion in a 5-hole GDi injector nozzle utilising E100, while combining both LES and URANS. The target is to develop an effective erosion diagnostic tool able to support, interpret and reduce the time and cost of durability tests.

The paper is structured as follows; first an overview of the observed erosion patterns appearing after 400 million injection cycles durability test on the GDi injector nozzle tip operated with E100 is provided. Then, the modelling approach is described in detail including the verification of the cavitation model against the Rayleigh collapse of a vapour bubble. Simulation results are then discussed and detailed information about the arising cavitation and the mechanisms behind the different erosion phenomena are provided, followed by a summary of the most important conclusions.

2. Injector durability tests and observed erosion patterns

The experimental campaign consisted of seven 5-hole injectors manufactured for the durability test submitted for durability analysis while operated with E100. The injector material is steel and the rail pressure in the tests was $350\,bar$. The hardware tests were performed at a temperature of, $T_{inj} = 40\,C^o$ and discharged into the ambient which corresponds to a back pressure of $p_{back} = 1\,atm.$ The operating conditions correspond to ethanol vapour saturation pressure of $p_{sat}(T_{inj}) = 17909\ Pa$, while the saturation temperature obtained at the downstream pressure is $T_{sat}(p_{back}) = 78\,C^o$ [71].

Therefore, ethanol is not injected in superheated state and the phase change under this conditions is driven by cavitation and not flash-boiling. The injections had an electrical pulse of $1\,ms$, and they were separated by $6\,ms$; the test was ran for 400 million injection cycles. The injection holes have a mean diameter of 170 μm and length-to-diameter ratio of $L/D \sim 1$. After the tests, several erosion patterns were found during inspection of the parts using scanning electron microscope (SEM). All parts showed damage in areas where cavitation is expected to form and develop. Figure 1 presents the SEM images for three of the injectors; more specifically damage at the injection hole inlet, sac volume entry, sac center and in the injector's sealing band (pintle needle valve seat) can be observed. Inspection of the injectors prior to the experiments confirmed that the sealing band a is not due to the manufacturing process.

3. Modelling approach

The compressible formulation of the Navier-Stokes equations is solved numerically using the commercial CFD code ANSYS Fluent [72]. The multiphase flow is simulated using a two-phase, three-component (fuel liquid, fuel vapour and air) homogeneous mixture model, where all phases are assumed to be in mechanical equilibrium while the flow is isothermal; thus, they share the same velocity and pressure. The flow is assumed isothermal and the energy conservation equation is not considered, only the non-condensable air is modelled not the dissolved part. A barotropic model has been implemented

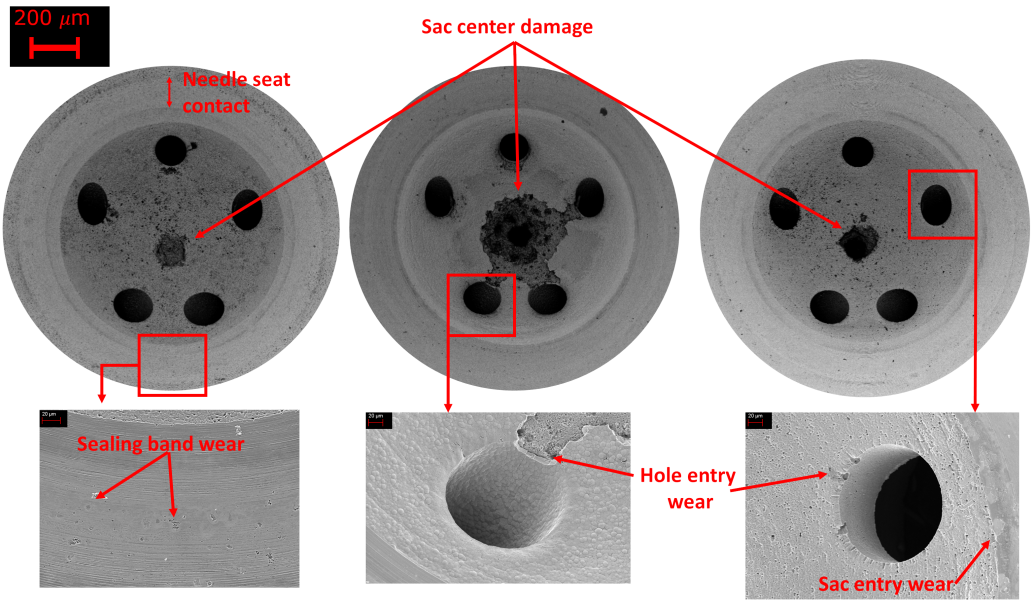

Figure 1: Damage patterns observed in a GDi nozzle after 400 M cycle durability test.

through a user defined function (UDF) specifying the variation of the fuel density as a function of pressure; additional UDFs are also used for accounting the needle valve movement and the cavitation induced surface erosion indicators.

3.1. Multiphase model

The physical properties appearing in the transport equations are determined by the corresponding values of the properties of the component phases in each control volume. Defining α_{fuel}, α_{air} as the volume fraction of fuel and air in a cell, respectively, the density in each cell is given by: $\rho = \alpha_{fuel}\rho_{fuel} + \alpha_{air}\rho_{air}$. Viscosity is computed using the same mixing rule between fuel and air, while it is assumed to be constant for each phase. Vis-

cous heating due to the high speed flow developing at the given pressure drop of 350 bar can lead to maximum variations in viscosity of 20% and density of 2.3%, respectively; this can be neglected as the resulting $\sim 20\%$ variation in the Reynolds number does not result in any change of the turbulent flow regime. The solved equations consist of the continuity and momentum equations for the mixture and the mass conservation equations for the air, where the volume constraint $\alpha_{fuel} + \alpha_{air} = 1$, in each cell must be respected:

$$\frac{\partial \rho}{\partial t} + \nabla \cdot (\rho \mathbf{v}) = 0 \tag{1}$$

$$\frac{\partial \rho \mathbf{v}}{\partial t} + \nabla \cdot (\rho \mathbf{v}\mathbf{v}) = -\nabla p + \nabla \cdot \bar{\bar{\sigma}} \tag{2}$$

$$\frac{\partial \alpha_{air}\rho_{air}}{\partial t} + \nabla \cdot (\alpha_{air}\rho_{air}\mathbf{v}) = 0 \tag{3}$$

The effective viscous stress tensor is defined as $\bar{\bar{\sigma}} = \tau + \tau_t = \mu(\nabla \mathbf{v} + (\nabla \mathbf{v})^T) + \tau_t$, where μ is the viscosity of the mixture and τ_t are the turbulent stresses estimated from the turbulence model used.

3.2. Turbulence model

In LES the flow structures that are dependent on the boundary conditions and the dimensions of domain simulated are termed as 'large' and are resolved by the numerical grid, while for the unresolved sub-grid scales, a physical

model is required This is achieved by filtering of the Navier-Stokes equations using a spatial low-pass filter determined by the cell size of the computational domain used. For compressible fluids the so-called Favre filter has to be adopted for the density and additional terms arise in the equations; these represent the sub-grid scale contributions to the equations of motion that have to be modelled [73, 74, 75]. The corresponding sub-grid scale model for the turbulent dissipation (viscosity) μ_t is the Wall-Adapting Local Eddy-Viscosity (WALE) model [76]. This model is capable of reproducing the turbulence wall behaviour ($\mu_t \sim o(y^3)$) and becomes 0 at $y = 0$, where y represents the normal distance to the wall. Another advantage is that it returns a zero turbulent viscosity for laminar shear flows (as opposed to widely used models such as the Smagorinsky model [77]). This is useful in the present application as it better resolves the flow during the start of the injection in the small gap between the needle valve and the housing; the flow is laminar and the introduction of additional viscosity would lead to incorrect prediction of shear and pressure losses

On the other hand, Reynolds-averaged Navier–Stokes (RANS) or unsteady RANS (URANS) provide the solution for the spatial and temporal mean flow variables at significantly reduced grid resolution as compared to LES. In the present work the $k-\omega$ SST model is employed; this is a blend between the standard $k-\varepsilon$ and $k-\omega$ models, and accounts two additional transport equations for modelling the turbulent kinetic energy (k) and its specific dissipation rate (ω); it offers better accuracy in the vicinity of walls

than the $k-\varepsilon$ and less sensitivity to the boundary conditions than the $k-\omega$ model [78] .

3.3. Cavitation model

The proposed polynomial barotropic cavitation model is similar to that presented in [79]. Given the vapour saturation pressure of the working fluid p_{sat} and a pressure interval δp over which the mass transfer takes place we can define:

$$\begin{aligned} p_{satL} &= p_{sat} + \frac{\delta p}{2} \\ p_{satV} &= p_{sat} - \frac{\delta p}{2} \end{aligned} \tag{4}$$

The fuel is in liquid state when $p > p_{satL}$ and follows a Tait equation of state (EOS):

$$\rho(p) = \rho_{satL} \left(\frac{p - p_{satL}}{B'} + 1 \right)^{1/n}, \; p \geq p_{satL} \tag{5}$$

The constants n and $B^{'}$ are dependent on the fluid and in the case of ethanol have been fitted from the density measurements of [80]. Figure 2 (left) shows the comparison of the fitted equation of state and the measured density data. Figure 2 (right) shows that the error of the fitting is below 0.03% for all pressures in the measurement range.

The model assumes a polytropic evolution of exponent γ_{vap} for the vapour fuel component (when $p \leq p_{satV}$) and a third order polynomial for the mixture (when $p_{satV} < p < p_{satL}$). A polytropic evolution is chosen for the vapour

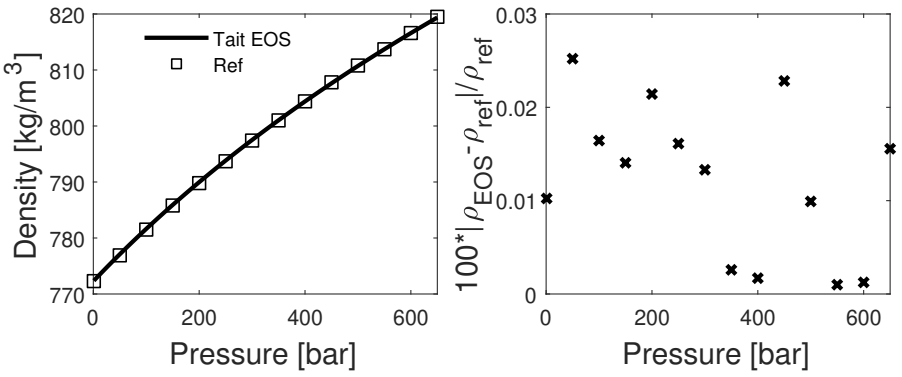

Figure 2: Comparison between the fitted Tait EOS and the density measurements of [80]. Desnity vs pressure (left) and % difference between fitted equation and measurements (right)

fuel component to allow for any exponent; in practice $\gamma_{vap} = 1$ has been used, effectively rendering the relationship isothermal ($p/\rho = RT = constant$). The full barotropic cavitation model proposed reads as:

$$\rho_{fuel}(p) = \begin{cases} \rho_{satL}\left(\frac{p-p_{satL}}{B'}+1\right)^{1/n} & p \geq p_{satL} \\ Ap^3 + Bp^2 + Cp + D & p_{satV} < p < p_{satL} \\ \left(\frac{p}{C_{vap}}\right)^{1/\gamma_{vap}} & p \leq p_{satV} \end{cases} \tag{6}$$

In the case of the vapour fuel component, the value of C_{vap} can be determined by knowing the vapour fuel density ρ_{satV} at pressure p_{satV} ($C_{vap} = p_{satV}/\rho_{satV}$). Although ρ_{satV} should not be a simulation tuning parameter, numerical trials have shown that using realistic low values of ρ_{satV} ($\rho_{satV}(p = p_{satV}, T_{inj}) = 0.14\,kg/m^3$ [71]) leads to difficulty in obtaining a numerically stable solution. Therefore a higher value has been used ($\rho_{satV} = 1.2\,kg/m^3$). Nevertheless, the simulation and modelling work of [15, 34] in high pressure

fuel injection systems show that using an ad-hoc higher vapour density does not prevent from obtaining accurate predictions of turbulent cavitating flows and cavitation erosion locations. Constants A, B, C, D for the mixture are unknown and they are calculated so that both density and speed of sound ($c^2_{fuel} = \frac{\partial p}{\partial \rho_{fuel}}$) are piecewise continuous by solving the following linear system of equations:

$$\begin{aligned} Ap^3_{satL} + Bp^2_{satL} + Cp_{satL} + D &= \rho_{satL} \\ Ap^3_{satV} + Bp^2_{satV} + Cp_{satV} + D &= \rho_{satV} \\ 3Ap^2_{satL} + 2Bp_{satL} + C &= 1/c^2_{satL} \\ 3Ap^2_{satV} + 2Bp_{satV} + C &= 1/c^2_{satV} \end{aligned} \tag{7}$$

This model presents a free parameter δp that regulates the maximum slope of the $p - \rho$ relationship and hence the minimum speed of sound in the mixture. In order to choose a physical value for δp it has to be taken into account that for homogeneous mixtures according to [7, 8], the minimum speed of sound should be between two extremes; the frozen speed of sound (also known in the literature as Woods or Wallis speed of sound) which is derived assuming no mass transfer and the equilibrium speed of sound (derived assuming infinitely fast heat exchange and mass transfer). Assuming realistic values at room temperature for the liquid and vapour of $c_L \approx 1100\,[m/s]$ and $c_V \approx 500\,[m/s]$ and taking the rest of the properties from [71] it can be shown that for a void fraction of 50%, $c_{frozen} = 2.02\,[m/s]$ and$c_{equilibrium}$=$0.17\,[m/s]$. The polynomial barotropic cavitation model with

Liquid properties		Vapour properties		Air properties	
ρ_{satL}	$772.3\ kg/m^3$	ρ_{satV}	$1.2\ kg/m^3$		
p_{satL}	$27909\ Pa$	p_{satV}	$7909\ Pa$		
n	11.09	γ_{vap}	1	γ_{air}	1.4
B'	$7.007 \times 10^7\ Pa$	C_{vap}	$6590\ Pa/(kg/m^3)$	C_{air}	$85708\ Pa/(kg/m^3)^{\gamma_{air}}$
c_{satL}	$1003.08\ m/s$	c_{satV}	$80.35\ m/s$		
μ_L	$8.22 \times 10^{-4}\ Pa\ s$	μ_V	$2 \times 10^{-5}\ Pa\ s$	μ_{air}	$2 \times 10^{-5}\ Pa\ s$

Table 1: Fluid properties of ethanol and air.

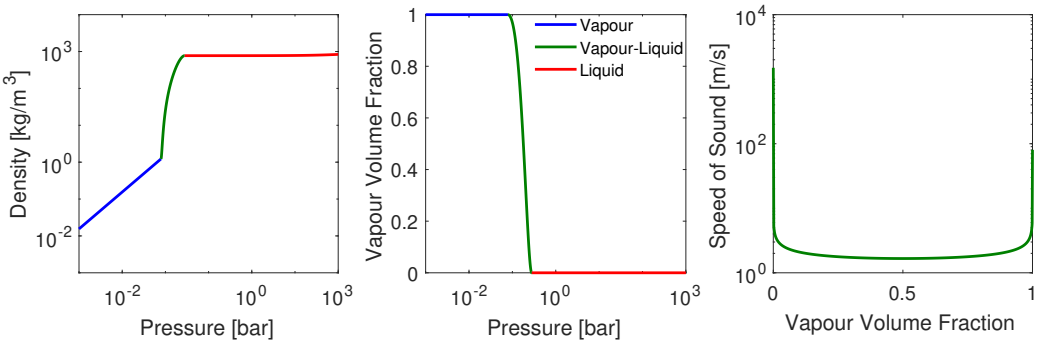

Figure 3: Polynomial barotropic EOS. Density (left), vapour volume fraction (middle), speed of sound vs vapour volume fraction (right).

the chosen δp returns a minimum speed of sound of $c_{min} = 1.7\,[m/s]$ which respects these bounds. The dependence of the fuel density, vapour volume fraction ($\alpha_{vap} = \frac{\rho_{satL} - \rho_{fuel}}{\rho_{satL} - \rho_{satV}}$) and speed of sound against pressure as well as the dependence of the speed of sound with the vapour volume fraction are all shown in Figure 3 in the case of pure fuel. Finally, the non-condensable air is modelled via an isentropic equation of state ($\rho_{air} = \left(\frac{p}{C_{air}}\right)^{1/\gamma_{air}}$), where the constant C_{air} is calculated at ambient conditions (1 bar and 293 K); see Table 1 for the values of all the constants related to the fuel properties. The calculation of α_{vap} when non-condensable air is present can be found in [34].

The model implementation has been verified against the Rayleigh spherical bubble collapse solution, describing the compression of a vapour bubble embedded in an infinite high pressure liquid. The assumptions under which this test case is valid are inviscid incompressible liquid, gravity and surface tension forces are neglected, the air content of the bubble is constant, its inertia is neglected and any exchange of heat with the surroundings is also neglected; the bubble is filled with saturated vapour whose partial pressure is the vapor pressure at the liquid bulk temperature. The interested reader is referred to the book of Franc for the derivations and further discussion [8]. The bubble wall collapse velocity is given in this case by:

$$\frac{dR}{dt} = -\sqrt{\frac{2}{3}\frac{p - p_{sat}}{\rho_L}\left[\left(\frac{R_0}{R}\right)^3 - 1\right]} \tag{8}$$

Where p is the far field pressure, p_{sat} is the vapour saturation pressure, ρ_L the liquid density, R_0 is the initial bubble radius and R is the bubble radius at time t. Integration of the previous equation yields an approximate collapse time of $\tau \approx 0.915 R_0 \sqrt{\frac{\rho_L}{p - p_{sat}}}$ for the collapse of a vapour bubble under the mentioned assumptions [8].

The model is verified for a 2D axis symmetric case, starting from a 20 μm radius bubble at p_{satV}, embedded in 100 bar liquid. The collapse time for the introduced polynomial cavitation model is 2.6% faster than the Rayleigh collapse and a maximum pressure in excess of 15000 bar is predicted at the

bubble centre after the collapse. Numerical tests have shown that using a 10 times smaller δp accelerates the bubble collapse time by 1.5%, at the expense of greatly reducing the stability of the solver

3.4. Moving mesh simulation methodology: mesh generation, boundary conditions and numerical setup.

The tested injector consists of a 5-hole GDi injector with nozzle hole diameter of 170 μm. The injectors are nominally identical; moreover, the injectors were inspected prior the durability tests and no difference between them due to manufacturing were identified. In the case of LES, due to its demanding computational time only a 72^o sector is simulated and periodic boundary conditions are considered (Figure 4 top). Pressure boundary condition are imposed at the inlet (350 bar) and at the outlet (101325 Pa). Since the use of periodic conditions in the LES sector model is a shortcoming, a URANS simulation is carried out for the full nozzle geometry.

The LES model setting is adapted from the basis of the previous studies on Diesel injection and primary breakup [81, 82, 83, 84, 29] and Gasoline [62, 85] injection and primary breakup simulations. In order to choose the appropriate filter/mesh size for the LES, the Taylor micro-scales (λ_g) is used [77]. This is an intermediate length scale at which fluid viscosity significantly affects the dynamics of turbulent eddies in the flow [86]. An estimation of the Reynolds number inside of the injection hole yields a value of $Re = \frac{(\rho V D)}{\mu} \sim$ 48000, in turn this corresponds to a $\lambda_g \sim D\sqrt{\frac{10}{Re}} = 2.45\ \mu m$. Consequently, a

fully hexahedral mesh was created with the aforementioned resolution in the regions of interest, namely the seat, sac and spray hole, and was progressively coarsened in the counter bore and discharge volume regions. Since resolution of the smallest eddies in the wall vicinity requires the distance between the wall and the cell centre position of the first cell layer non-dimensionalised based on the friction velocity to be of the order of 1 ($y^+ \sim 1$) [77], additional refinement is applied in the wall region. A mesh size of $\sim 0.5\ \mu m$ is used close to the walls. The average y^+ is about 1 in the region of interest and the maximum wall y^+ is about 10 around the sharp edge of the spray hole entrance. This results in a mesh count of 2.3 M elements for a geometrical sector in the LES case. The authors reported in [29] different LES quality metrics confirming the suitability of the mesh design method for a Diesel pilot injection and for conciseness these quality metrics are not reported here. In the URANS case, the resolution requirements are relaxed and a 2.7 M fully hexahedral mesh is employed for the full nozzle. This mesh resolution has been verified to be able to predict the mass flow rate at full lift and different injector designs with an accuracy of 3%, also it was verified that the change in vapour volume fraction at the nozzle exit was within an acceptable range of 1% with further mesh refinement; again for conciseness these results are not reported here. Table 2 presents the summary of the employed meshes for LES and URANS simulations as well as a CPU time of the presented simulations.

A node interpolation technique has been chosen for the moving mesh sim-

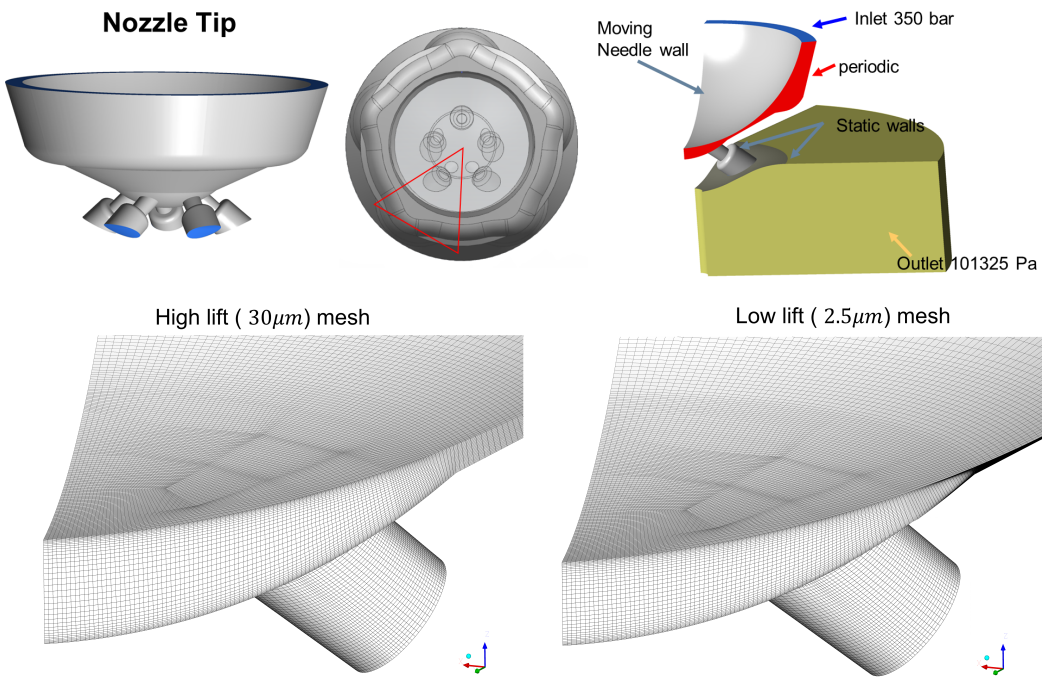

Figure 4: Simulation domain and boundary conditions (top) and LES mesh (bottom). Selected 72^osector for sector nozzle geometry simulation highlighted by a red triangle. LES mesh details for both $30\mu m$ lift (bottom-left) and low lift (bottom-right)

	LES 72^o sector mesh	URANS full nozzle mesh
Mesh count	$2.3M$	$2.7M$
# of cells across the hole diameter	105	57
Near wall resolution in the hole [μm]	0.5	1
Characteristic mesh size in the hole [μm]	2	4
Time step [s]	5×10^{-9}	5×10^{-8}
CPU time [CPU hours]	$50\,days \times 60\,cpu \approx 72000$	$5\,days \times 60\,cpu \approx 7200$

Table 2: Mesh details.

ulation already utilised by the authors in [62, 29]. This requires to generate two topologically identical meshes, one for the highest lift and one for the lowest. Node positions in the mesh are then interpolated between these two extreme values according to an imposed needle lift profile. The imposed needle profile is taken from a 1D injector model simulation. Only a ballistic opening and closing are considered with a maximum needle lift of 30 μm and a minimum lift of 2.5 μm. For a detail of the LES meshes see Figure 4 bottom. For lifts under 2.5 μm the needle motion is stopped and an interior interface pre-defined at the sealing surface (surface of minimum distance between needle and housing) is changed to a wall separating the upstream part from the downstream region. The force that the needle valve exerts on the housing leads to elastic deformation and therefore the contact area between the two surfaces is a band of finite width [87]. However, in the current model this deformation is not modelled and the contact line between both surfaces is a single circle.

The solver selected is the coupled pressure-based solver available in ANSYS Fluent[88]. In terms of the discretization scheme for the momentum equation, the second order upwind is used in the URANS case [89]. In the LES case, a second order bounded central differencing scheme (hybrid between central and second order upwind based on the normalized variable diagram (NVD) approach together with the convection boundedness criterion (CBC) following the work of [90], [72]) was used for momentum discretization; this scheme has small numerical dissipation and sufficient numerical

stability for LES simulations [91]. For all simulations a body-force-weighted scheme is employed for pressure interpolation [72] while for the density interpolation a first order upwind scheme [89] is used. Finally, the calculation of the gradients was done using the Least Squares Cell-Based method.

The used solver is pressure-based and therefore the simulation stability is not limited by the acoustic wave propagation time scale. However, temporal resolution for LES requires minimum diffusion for the advection of the turbulent eddies. Therefore, a time step of 5×10^{-9} s is chosen for the LES case, yielding a convective $CFL \sim 1$ in the spray hole. For the URANS cases, a time step of 5×10^{-8} s is selected resulting in a convective $CFL \sim 5$ in the spray hole. One LES injection cycle and two successive URANS injection cycles have been simulated. The pressure field is initialised with 350 bar above the sealing band and with 101325 Pa downstream. Air volume fraction is set to 1 below the sealing and to zero above in the LES case and the first URANS injection. A second URANS injection is carried out as a continuation of the final flow calculated at the end of the previous injection cycle.

3.5. Cavitation erosion indicator

Selection of the most relevant criteria for the evaluation of cavitation erosion is an active research topic. In the current work three parameters have been tested and compared against the experimental observations:

1. The maximum pressure recorded throughout the simulation on the walls, $max(p(t))$, as used by[15, 34, 92] in moving needle Diesel fuel

injector nozzle flow simulations.

2. The accumulated total derivative of the pressure field on the walls $\int(\frac{Dp}{Dt})^+dt$, where $\left(\frac{Dp}{Dt}\right)^+ = max(\frac{Dp}{Dt}, 0)$, used in [13]. As noted in this study, the use of the Lgrangian derivative stems from the fact that cavitation bubbles at the final collapse stages follow the flow streamlines and therefore total derivatives apply to both quasi-steady and unsteady flows. This indicator implies that a steeper pressure variation leads to more violent cavitation collapse. This indicator is similar to the Intensity Function Method (IFM) of [65] and the maximum pressure time derivative recorded on the wall and employed by [14].

3. The accumulated radiated power on the wall due to vapour collapse $\int \frac{De}{Dt}dt$, which was previously used in [63, 93]. Details on the definition of the radiated power due to cavitation collapse are given in the remaining part of this section.

The potential energy available in a spherical bubble of radius R_0 is [94, 93]:

$$E = \frac{4}{3}\pi R_0^3(p_d - p_v)\,[J] \tag{9}$$

where, p_d is the ambient pressure driving the collapse and p_v is the vapour pressure inside the bubble. For a cavity with arbitrary shape the potential energy per unit volume can be approximated by [63, 93]:

$$e = \alpha_{vap}(p_d - p_v)\,[J/m^3] \tag{10}$$

The change per unit time of this last parameter is the specific power radiated due to a collapsing vapour cavity and can be expressed as:

$$\frac{De}{Dt} = \frac{D\alpha_{vap}}{Dt}(p_d - p_v) + \alpha_{vap}\frac{Dp_d}{Dt}\,[W/m^3] \tag{11}$$

where, $\frac{D()}{Dt} = \frac{\partial()}{\partial t} + \mathbf{v}\nabla()$. However, as discussed in [93] assuming that only power is radiated when condensation takes place only the first term in Eq. 11 contributes to the radiated power and only if the material derivative of α_{vap} is negative. Therefore the radiated power by collapsing cavitation structures can be expressed as:

$$\frac{De}{Dt} = \left(\frac{D\alpha_{vap}}{Dt}\right)^{-}(p_d - p_v)\,[W/m^3] \tag{12}$$

where, $\left(\frac{D\alpha_{vap}}{Dt}\right)^{-} = min(\frac{D\alpha_{vap}}{Dt}, 0)$. In order to evaluate $\frac{De}{Dt}$, p_d remains to be defined. As pointed out in [93, 49], its definition is not trivial since the driving pressure for a cavity is not a local magnitude but rather the pressure "far away" from the bubble. Exactly defining what is "far away" is left by [49] as an open research question. In our case the choice made has been the average pressure surrounding the vapour for each computational cell, as we found reasonable that the difference between this average and the cell pressure is driving the changes in vapour volume fraction inside the computational cell. Therfore, it has been assumed that p_d can be estimated by the averaged pressure over the cell faces of all neighbouring computational cells, i.e. $p_d = \frac{\sum_i p_i A_i}{\sum_i A_i}$, where the summations are extended to all

the neighbouring cells with pressure p_i and shared face area A_i. Assuming that cavitation damage is caused by cumulative loading of the nozzle walls, the aforementioned cavitation erosion indicators have been implemented into Fluent through user defined functions.

The accumulated erosive power as used in the current study only takes into account the power accumulated in the first grid cell neighbouring to the wall, although for static meshes it is possible to transfer the accumulated load of the whole domain to the walls [49], this has still not been devised for moving meshes and was not considered in the present study. Also, this paper does not consider the coupling of the cavitation erosion indicators with the material properties of the metals nor the coupling of the erosion indicators with the solid material; this is out of the scope of the current study.

4. Results and discussion

Flow characterisation

The evolution of the void fraction inside the sac volume and the injection holes for both the vapour fuel component and the air together with the imposed needle profile is shown in Fig. 5 for both the LES sector nozzle geometry (solid line) and the URANS simulations (dotted lines). It can be observed that during the needle opening phase, air is pushed out of the sac volume due to its filling with fuel and that vapour is created.

A time sequence of the evolution of the liquid volume fraction field and the velocity field on a plane normal to the orifice and the 3D iso-surfaces

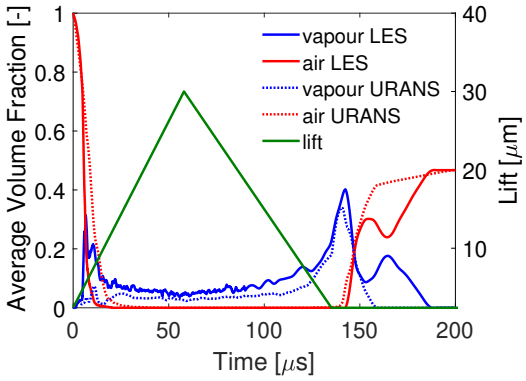

Figure 5: Volume fraction of air (red) and vapour (blue) inside the sac and orifices against time. Needle lift against time (green). LES sector nozzle geometry (left) and URANS full nozzle geometry 1^{st} injection cycle (right).

of vapour volume fraction 10% (black) and air volume fraction 50% (magenta) are shown in Fig. 6 for both the LES sector nozzle (top) and the URANS simulation (bottom). In the liquid volume fraction field visualisations the areas of $p < p_{satL}$ and $\alpha_{vap} > 0$ are represented in black to provide a sharp visualisation of the areas where cavitation is present. High speed liquid coming from the needle seat area ($t = 2.5\,\mu s$) flows towards the sac volume center and recirculates ($t = 5\,\mu s$). This recirculation results in low pressure regions and the creation of vapour. Cavitation is also present in the small gap between the housing and the needle valve, where the flow is throttled. The LES simulation presents higher peak velocities compared to the URANS simulation and therefore the amount of vapour created due to the recirculation in the sac volume is also higher (see Fig. 5). The liquid is progressively directed towards the injection holes pushing the air out of the injector ($t = 10\,\mu s$). In the case of the LES the flow in the sac volume

becomes a complex liquid, vapour and air mixture with finer structures than in the URANS case.

A time sequence of the flow as it further develops during the needle valve opening for both simulations is presented in Fig. 7. As the needle lift increases, the cavitation present in the small gap at the sac entry recedes. The air in the sac volume is evacuated and the flow enters the injection hole first from the sac side, until the air is purged from the sac volume ($t = 12.5\,\mu s$) and then from the seat side ($t = 15\,\mu s$). Eventually, cavitation is mostly constrained to the injection holes ($t = 32.5\,\mu s$). This cavitation arises due to flow separation at the injection hole inlet where a cavitating shear layers is formed ($t = 15\,\mu s$ and $t = 32.5\,\mu s$).

The full nozzle geometry configuration results in hole-to-hole interactions leading to vortices connecting adjacent holes, which can be sufficiently strong to cavitate, see Fig.8 where the vortices represented by the Q-criterion; the 10% vapour volume fraction are simultaneously depicted for the full nozzle URANS geometry at $t = 32.5\,\mu s$. This is a typical phenomenon in swirling flow conditions, known as string cavitation where cavitation can happen in the core of large scale vortices and has been previously discussed for both Diesel fuel [31, 32, 33] and GDi[69] nozzles.For the remaining needle opening phase, cavitation remains constrained to the holes until the needle closing phase.

In Fig. 9 the snapshots of the flow just before and after the needle valve closing are shown for both simulations. Shortly before the needle valve

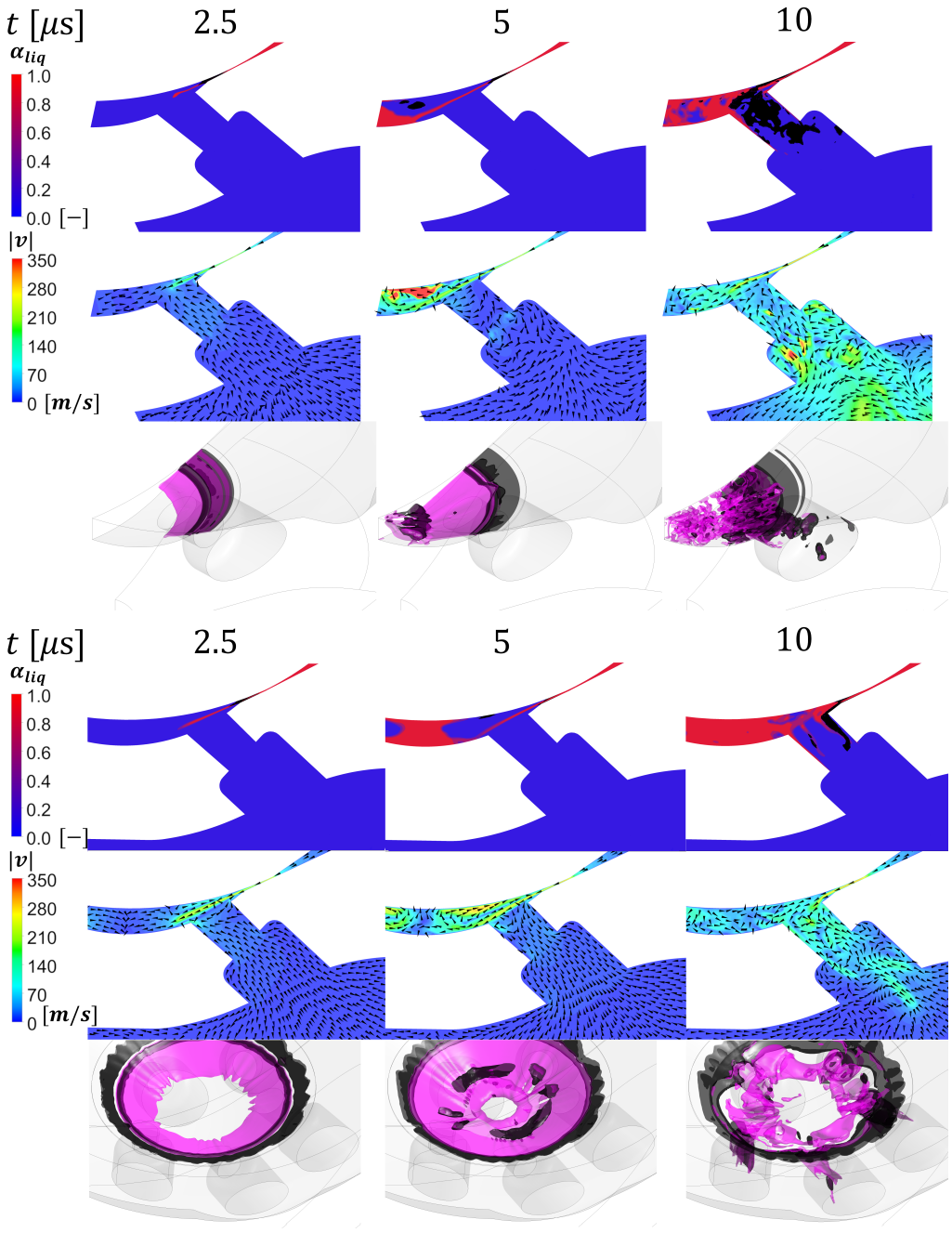

Figure 6: Time sequence for the start of injection. LES results (top) URANS results (bottom). For each modelling approach: liquid volume fraction in a plane perpendicular to the orifice with regions of $p < p_{satL}$and $\alpha_{vap} > 0$ in black (top), velocity magnitude field and velocity vectors in the same plane (middle) and 3D iso-surfaces of vapour volume fraction 10% (black) and air volume fraction 50% (magenta) (bottom).

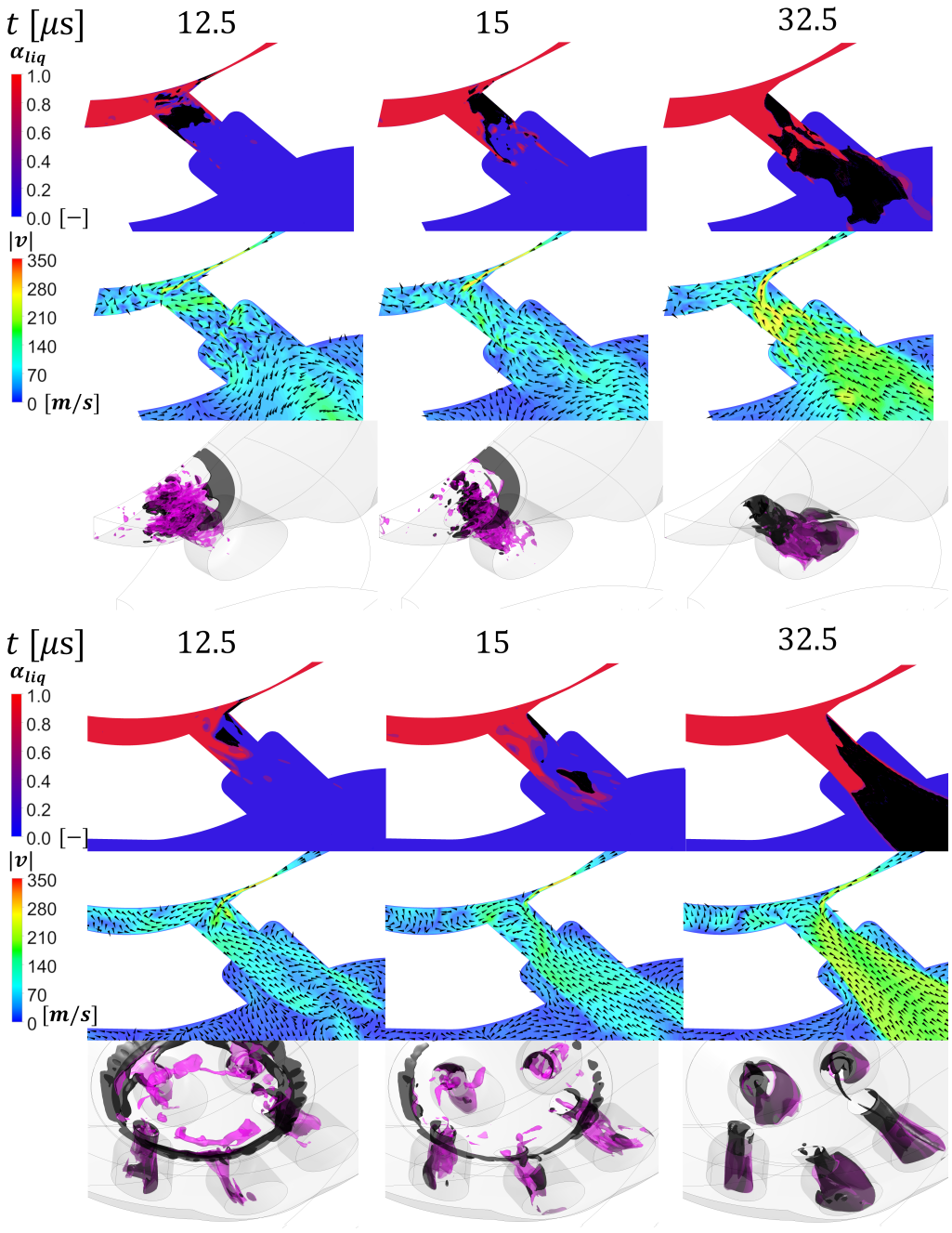

Figure 7: Time sequence for the needle opening phase. LES results (top) URANS results (bottom). For each modelling approach: liquid volume fraction in a plane perpendicular to the orifice with regions of $p < p_{satL}$and $\alpha_{vap} > 0$ in black (top), velocity magnitude field and velocity vectors in the same plane (middle) and 3D iso-surfaces of vapour volume fraction 10% (black) and air volume fraction 50% (magenta) (bottom).

Figure 8: URANS full nozzle hole-to-hole interaction. Vortex structures depicted by Q-criterion iso-surface (gold) and 10% vapour volume fraction iso-surface black in the sac volume and injection holes at $t = 32.5\mu s$.

closure ($t = 135\,\mu s$), cavitation in the small gap between the needle and the housing wall reappears. The needle valve closes at $t = 135.1\,\mu s$. Just after the needle closing, a ring of vapour is created which then collapses towards sealing ($t = 137.5\,\mu s$ and $t = 140\,\mu s$). Additionally, due to the relative high momentum in the injection hole, the sac pressure drops and the fuel cavitates causing big vapour bubbles to appear inside the nozzle's sac volume.

The final evolution of the flow is shown in Fig. 10. When the flow in the injection hole sufficiently decelerates, the vapour in the injection hole starts to collapse entraining air into the injector ($t = 145\,\mu s$ and $t = 150\,\mu s$). The LES and URANS simulations present differences for the final collapse phase of the vapour. The LES sector model predicts a vapour bubble in the sac

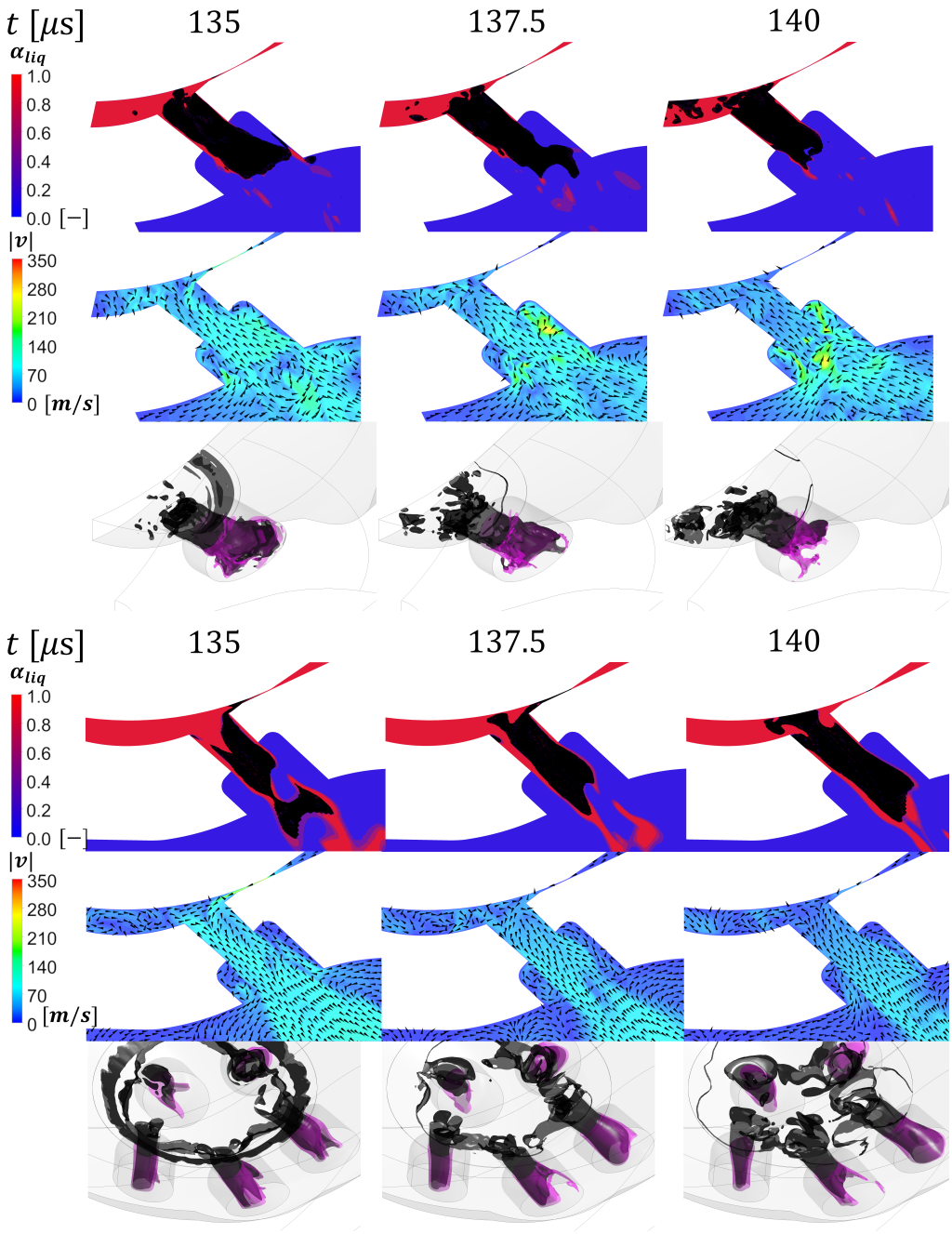

Figure 9: Time sequence for the needle closing phase. LES results (top) URANS results (bottom). For each modelling approach: liquid volume fraction in a plane perpendicular to the orifice with regions of $p < p_{satL}$and $\alpha_{vap} > 0$ in black (top), velocity magnitude field and velocity vectors in the same plane (middle) and 3D iso-surfaces of vapour volume fraction 10% (black) and air volume fraction 50% (magenta) (bottom).

volume to be perfectly centered in the injector axis. This yields a fast focused collapse of the vapour in the sac center ($t = 145\,\mu s$ to $t = 150\,\mu s$), which is followed by a rebound ($t = 160\,\mu s$) before the vapour finally collapses and vanishes ($t = 190\,\mu s$), see also Fig. 5. On the other hand, the URANS full nozzle model predicts an asymmetric structure which presents a less focused collapse with no rebound.

Regardless of the modelling approach, vapour collapse in the sac volume center is predicted and a similar fraction of the sac volume and injection hole is occupied by air at the end of the injection (46.7% LES and 46.9% URANS). This suggests that the sac volume is not full of air between injections and that some residual liquid is present. This observation has been seen in previous works in the literature, see for example[29]. Therefore, a second URANS full nozzle simulation was carried out starting from the results $65\,\mu s$ after needle closure of the first injection. Fig. 11 depicts the evolution of the volume fraction of the sac volume and injection holes filled with air (red) and vapour (blue) for both injections against time. Flow visualisations for the second URANS opening are shown in Fig. 12. During the second needle valve opening, the residual liquid in the sac volume cavitates due to the fast needle opening resulting pressures lower than the fuel's vapour pressure as the needle valve lifts ($t = 2.5\,\mu s$ and $t = 5\,\mu s$); this causes a greater amount of vapour to be created compared to the first injection, as seen in Fig. 11. Moreover, during the second injection the residual liquid existing in the sac makes the high speed liquid coming from the needle valve seat to penetrate

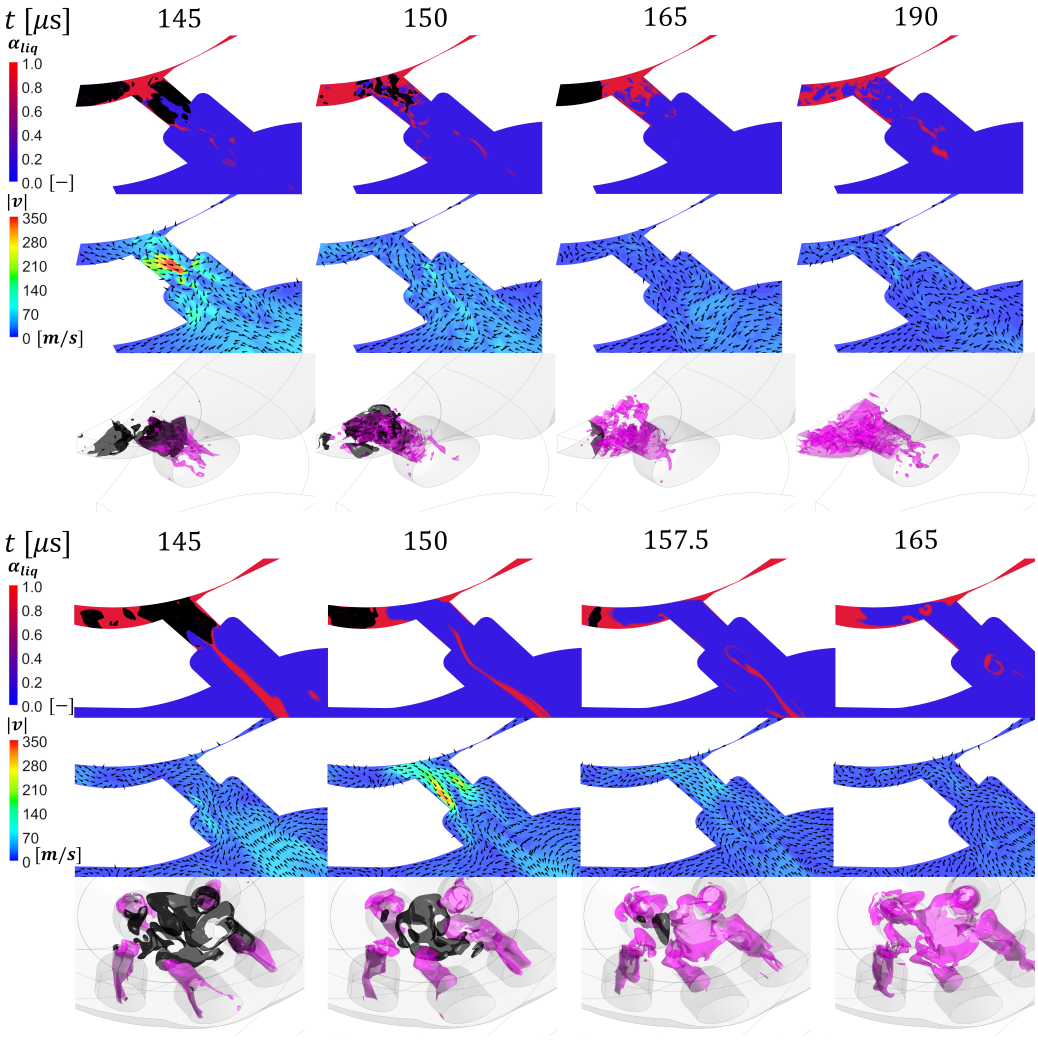

Figure 10: Time sequence for the flow after the needle closure. LES reuslts (top) URANS results (bottom). For each modelling approach: liquid volume fraction in a plane perpendicular to the orifice with regions of $p < p_{satL}$and $\alpha_{vap} > 0$ in black (top), velocity magnitude field and velocity vectors in the same plane (middle) and 3D iso-surfaces of vapour volume fraction 10% (black) and air volume fraction 50% (magenta) (bottom).

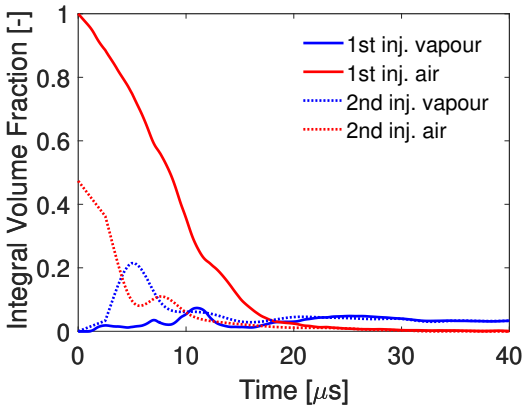

Figure 11: Volume fraction of air (red) and vapour (blue) inside the sac and orifices against time for the first (solid) and second (dotted) URANS injection.

less into the sac volume before it starts to recirculate towards the injection holes ($t = 5\,\mu s$ and $t = 10\,\mu s$). $20\,\mu s$ after the start of injection, no major differences between the first and second injections are observed; the same phenomena during the needle closing and after the injection are predicted.

Assessment of cavitation erosion prone locations

In this section the results obtained for the cavitation erosion indicators previously described in section 3.5 are presented for both the LES sector nozzle geometry simulation and the second URANS event. Fig. 13 shows the maximum pressure recorded throughout the simulation ($max(p(t))$), $\int (Dp/Dt)^+ dt$, and $\int (De/Dt) dt$ on the injector wall. In the LES case $max(p(t))$ returns high values in the area where the flow recirculates during the injector opening, inside the injection hole, in the region upstream of the injection hole and in the injector axis region. The maximum pressures detected are of the order of $\sim 1500 bar$ in the needle sealing area. In the case of URANS, $max(p(t))$ does

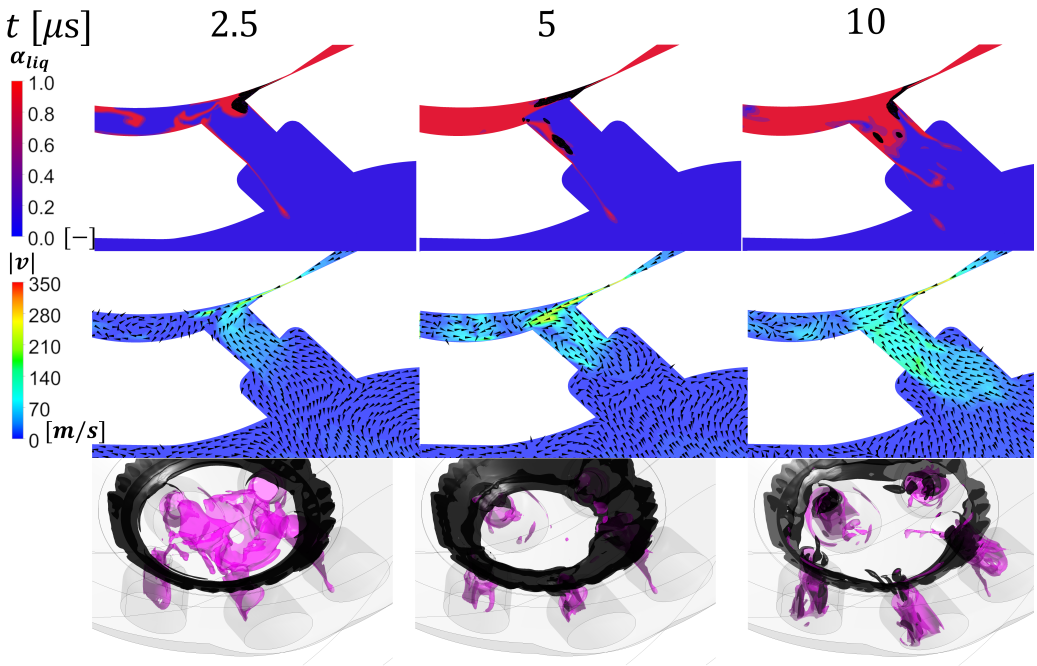

Figure 12: Flow visualisations for the opening of the second URANS injection. Liquid volume fraction in a plane perpendicular to the orifice with regions of $p < p_{satL}$and $\alpha_{vap} > 0$ in black (top), velocity magnitude field and velocity vectors in the same plane (middle) and 3D iso-surfaces of vapour volume fraction 10% (black) and air volume fraction 50% (magenta) (bottom).

not provide sufficient contrast to identify any erosion prone location. For the LES case $\int(Dp/Dt)^{+}dt$, returns high values at the injection hole inlet and the injector axis region, while the URANS simulation returns high values at the inlets of the injection holes and between the two holes which were identified to be strongly interacting with cavitating vortex strings; there is also a hint of high values towards the needle valve sealing area. The final indicator,$\int(De/Dt)dt$, presents high values in the LES case at the injection hole inlet, sac volume entry corner, needle valve sealing band region and sac volume centre region. In the URANS simulation the same areas of high $\int(De/Dt)dt$ are identified but the sac volume center region shows a more dispersed pattern. Overall, the indicators point at high cavitation erosion risk in the needle valve sealing band, sac volume entry corner, hole entry and sac volume centre regions, which were the areas that presented wear according to the durability tests (see Fig. 1). Sector model URANS results not reported here for conciseness do show high erosive power at the sac centre; therefore, the high-risk hot spot at the sac centre can be an artefact of considering only a sector instead of the full nozzle geometry.

In the LES simulation$\int(Dp/Dt)^{+}dt$, presents the least areas with agreement with the hardware test, while $max(p(t))$ and $\int(De/Dt)dt$ identify very similar erosion risk areas. In the URANS simulation $max(p(t))$ presents no agreement with the hardware test, $\int(Dp/Dt)^{+}dt$ shows moderate agreement in the orifice inlets and $\int(De/Dt)dt$ identifies as erosion risk areas the regions that showed damage in the hardware tests. Tables 3 and 4 show a summary

of the correlations found between the indicators and the hardware tests for the LES sector nozzle modelling and the URANS full nozzle modelling, respectively.

It has to be noticed that $\int (Dp/Dt)^+ dt$ accounts for all changes in pressure, not only those coming from vapour collapse; regions with unstable flow can present high pressure derivatives that may not always be attributed to the collapse of vapour structures. On the other hand, De/Dt implicitly accounts exclusively for the pressure derivatives arising from cavitation collapse,

$$\frac{De}{Dt} = (p_d - p_v)\Big(\frac{D\alpha_{vap}}{Dt}\Big)^- = -\frac{p_d - p_v}{\rho_{satL} - \rho_{satV}}(\frac{D\rho}{Dt})^+ = -\frac{p_d - p_v}{\rho_{satL} - \rho_{satV}}\frac{1}{c^2}(\frac{Dp}{Dt})^+$$

and therefore it is expected to present higher correlation with the experimentally observed damage. Regarding $max(p(t))$, the work of [95] shows that the cavitation collapse pressure is inversely proportional to the cell size at the collapse centre but that the location of collapse events is not affected by grid resolution, but although this affects the peak pressure in the domain the value recorded at the wall should be less affected [52]. Concerning the URANS modelling approach employed in this study, the higher effective flow viscosity and higher time resolution result in pressure peaks that are indistinguishable from the injection pressure but with the same cavitation locations than the more finely resolved LES. A discussion on the effect of time resolution on the pressure peaks due to cavitation collapse can be found in

Region	Parameter		
	$max(p(t))$	$\int(Dp/Dt)dt$	$\int(De/Dt)dt$
Sealing band	Good	Poor	Good
Sac entry corner	Good	Poor	Good
Injection hole inlet	Good	Good	Good
Sac volume center	Good	Good	Good

Table 3: LES sector nozzle modelling. Correlation to hardware tests of the cavitation erosion indicators evaluated.

Region	Parameter		
	$max(p(t))$	$\int(Dp/Dt)dt$	$\int(De/Dt)dt$
Sealing band	Poor	Some	Good
Sac entry corner	Poor	Poor	Good
Injection hole inlet	Poor	Good	Good
Sac volume center	Poor	Some	Some

Table 4: URANS full nozzle modelling. Correlation to hardware tests of the cavitation erosion indicators evaluated.

[96]. Eventhough in LES the choice of indicator is less important, since the flow and pressure is better resolved, for the particular problem under study $\int(De/Dt)dt$ seems to be the most appropriate indicator as it depends on the cavitation locations, which are less affected by grid resolution and it implicitly accounts for the pressure variations induced by cavitation collapse. This is in spite of the definition of $\int(De/Dt)dt$ being grid dependent and only taking into account the accumulated power in the first layer of cells neighbouring with the wall.

Erosion development process over one injection cycle

Next, further insight about how the damage develops during an injection event is given based on the results for the second URANS injection as it

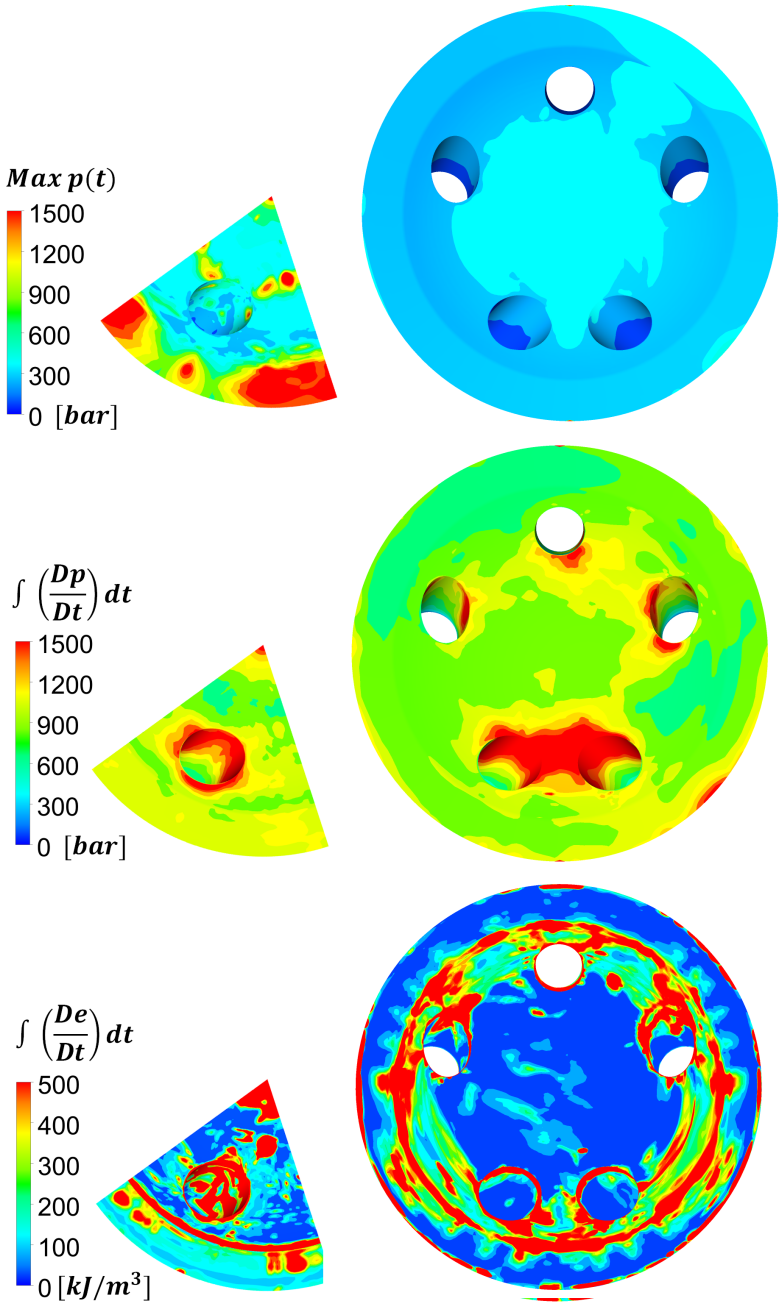

Figure 13: Cavitation erosion indicators on the injector wet wall for the LES sector nozzle geometry (left) and the URANS full nozzle (right). Only the region downstream of the sealing is shown. Maximum pressure recorded throughout the simulation (top), $\int(Dp/Dt)dt$ (middle) and $\int(De/Dt)dt$ (bottom) on the injector wet wall.

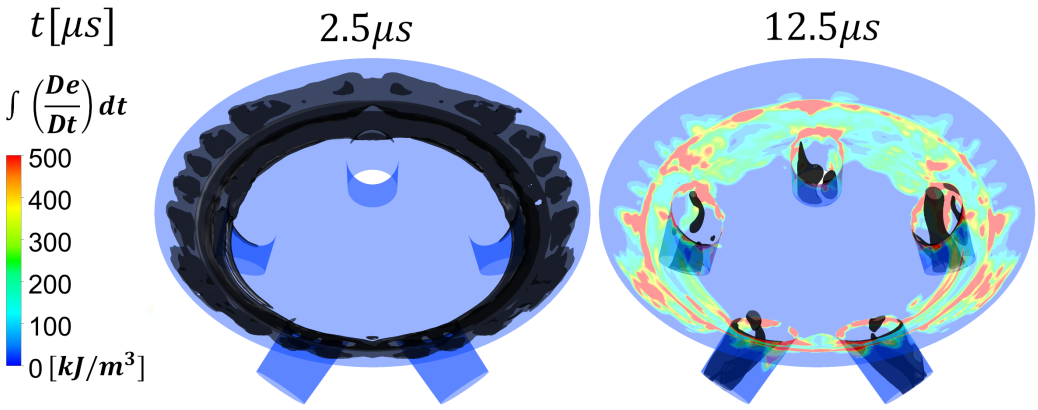

Figure 14: Mechanism for sac volume entry wear. 10% fuel vapour volume fraction iso-surface (black) and injector nozzle wall coloured by $\int_{t=0}^{t=t_0}(De/Dt)dt$, where $t_0 = 2.5\,\mu s$ (left) and $t_0 = 12.5\,\mu s$ (right).

is deemed to have more realistic initialisation than the first injection event. Fig.14 presents how the erosion at the sac volume inlet corner arises at the beginning of the injection. The 10% fuel vapour volume fraction iso-surface and the nozzle wall coloured by the value of $\int_{t=0}^{t=t_0}(De/Dt)dt$, (where $t_0$is the simulation time) are shown for two instants during the needle valve opening phase. When cavitation at the sac volume entry disappears, radiated power due to cavitation accumulates in the sac entry area. A similar erosion pattern was also observed experimentally in the case of Diesel injection in [97].

Further evidence of how the sealing band damage is occurs is depicted in Fig.15. This wear is caused by the ring of vapour created just after the needle closing. This structure collapses towards the sealing band and radiated power accumulates in the sealing band region

Finally, Fig.16 shows the mechanism behind the sac volume centre wear. It can be attributed to repeated loading of the sac volume wall over many

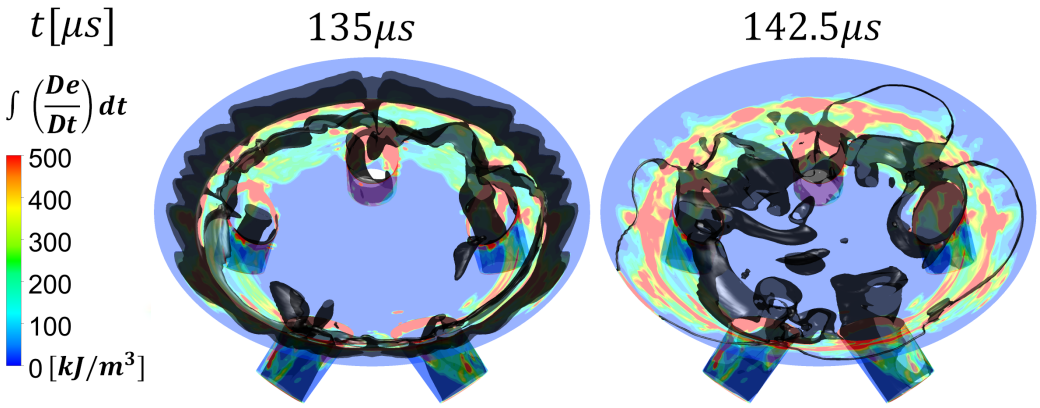

Figure 15: Mechanism for sealing band wear. 10% fuel vapour volume fraction iso-surface (black) and injector nozzle wall coloured by $\int_{t=0}^{t=t_0}(De/Dt)dt$, where $t_0 = 135\,\mu s$ (left) and $t_0 = 142.5\,\mu s$ (right).

injection cycles due to the asymmetric collapsing vapour structure predicted at the end of the injection. However, the high sac centre damage in the hardware tests might be caused by events not represented in the simulations, such as the quick needle opening when the sac is filled with liquid or the off-centred needle valve closure. Also, the relative damage at the needle seat area could potentially be affected by the sealing treatment; future work could include the modelling of the contact between the needle seat and injector housing such ass [98].

5. Conclusions

Modelling of the cavitating flow in prototype 5-hole GDi injectors operated with E100 fuel has been presented. Erosion sites were identified for all injectors tested in areas where cavitation is forming during hardware durability tests after 400 million cycles.

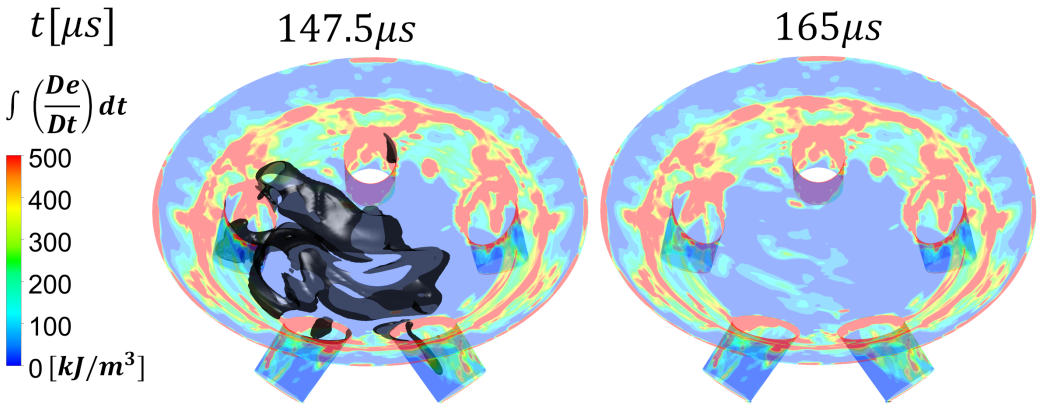

Figure 16: Mechanism for sac volume center wear. 10% fuel vapour volume fraction iso-surface (black) and injector nozzle wall coloured by $\int_{t=0}^{t=t_0}(De/Dt)dt$, where $t_0 = 147.5\,\mu s$ (left) and $t_0 = 165\,\mu s$ (right).

Both URANS for the whole 5-hole nozzle geometry and LES restricted only to a sector of one hole, were employed for the simulation of the internal nozzle flow; cavitation was considered through a barotropic model linking the density of liquid and vapour over the range of pressures examined using a smooth polynomial interpolation. The model predicts accurately the speed of sound of a wide range of Mach numbers and thus, the collapse of vapour cavitation structures during the opening and closing of the injector's needle valve. LES predicted overall higher peak pressure values during cavitation collapse, compared to URANS, while different collapse characteristics have been observed after the needle valve closing. Still, incorporation of the full nozzle geometry in URANS revealed that the residual liquid remaining in the sac volume in between successive injection events is prone to cavitate due to the pressure drop caused by the sudden valve closure. In an effort to predict locations on the nozzle geometry prone to cavitation erosion, three

cavitation erosion indicators have been implemented into the flow solver. Out of those, the indicator linked with the accumulated erosive power was found to correlate better against the obtained experimental data from the corresponding durability tests.

Acknowledgments

The European Union Horizon-2020 Research and Innovation Program funding to the PhD project of Eduardo Gomez Santos (No 675676), the FNR funding to the PhD project of Ramesh Venkatasubramanian (No 12553319), the ANSYS HPC research license grant to Delphi Technologies, and the CPU time granted by Gompute are highly appreciated. The authors would like to thank Dr. Walter Piock for opening this research topic, as well as the technical discussions and support to the realisation of the work, and to Kevin Allen, Jeremy Siegfried and the rest of the Delphi Technologies colleagues involved in providing the durability hardware test images.

References

[1] R. D. Reitz, H. Ogawa, R. Payri, T. Fansler, S. Kokjohn, Y. Moriyoshi, A. Agarwal, D. Arcoumanis, D. Assanis, C. Bae, K. Boulouchos, M. Canakci, S. Curran, I. Denbratt, M. Gavaises, M. Guenthner, C. Hasse, Z. Huang, T. Ishiyama, B. Johansson, T. Johnson, G. Kalghatgi, M. Koike, S. Kong, A. Leipertz, P. Miles, R. Novella, A. Onorati, M. Richter, S. Shuai, D. Siebers, W. Su, M. Trujillo,

N. Uchida, B. M. Vaglieco, R. Wagner, and H. Zhao, "Ijer editorial: The future of the internal combustion engine," *International Journal of Engine Research*, vol. 21, no. 1, pp. 3–10, 2020. https://doi.org/10.1177/1468087419877990.

[2] L. Zigan, J. Shi, I. Krotow, I. Schmitz, M. Wensing, and A. Leipertz, "Fuel property and fuel temperature effects on internal nozzle flow, atomization and cyclic spray fluctuations of a direct injection spark ignition injector," *International Journal of Engine Research*, vol. 14, no. 6, pp. 543–556, 2013.

[3] K. Makri, R. Lockett, and M. Jeshani, "Dynamics of post-injection fuel flow in mini-sac diesel injectors part 1: Admission of external gases and implications for deposit formation," *International Journal of Engine Research*, 2020. https://doi.org/10.1177/1468087419895425.

[4] F. Black, "An overview of the technical implications of methanol and ethanol as highway motor vehicle fuels," in *SAE Technical Paper*, SAE International, 1991. https://doi.org/10.4271/912413.

[5] F. A. GodÃnez, M. Navarrete, O. ChÃ¡vez, and E. GuzmÃ¡n, "Transient Cavitation by Quick Closing Pincers," in *Proceedings of the 10th International Symposium on Cavitation (CAV2018)*, ASME Press, 2018.

[6] F. Godinez, R. Mayen-Mondragon, J. Guzman, O. Chavez, M. Gavaises, and R. Montoya, "Bioinspired snapping-claw apparatus to study hydro-

dynamic cavitation effects on the corrosion of metallic samples," *Review of Scientific Instruments*, vol. 91, p. 066101, 2020.

[7] C. Brennen, *Cavitation and bubble dynamics*. Oxford: Oxford University Press, 1995.

[8] J. P. Franc and J. M. Michel, *Fundamentals of Cavitation*. Kluwer Academic Publishers, 2005.

[9] A. Shima, K. Takayama, Y. Tomita, and N. Oshawa, "Mechanism of impact pressure generation from spark-generated bubble collapse near a wall," *AIAA Journal*, vol. 21, no. 1, pp. 55–59, 1983. https://doi.org/10.2514/3.8027.

[10] E. A. Brujan, D. S. Hecht, F. Lee, and G. A. Williams, "Properties of luminescence from laser-created bubbles in pressurized water," *Phys. Rev. E*, vol. 72, p. 066310, 2005. https://doi.org/10.1103/PhysRevE.72.066310.

[11] R. Lockett and A. Bonifacio, "Hydrodynamic luminescence in a model diesel injector return valve," *International Journal of Engine Research*, 2019. https://doi.org/10.1177/1468087419870421.

[12] T. Terwisga, E. Van Wijngaarden, J. Bosschers, and G. Kuiper, "Achievements and challenges in cavitation research on ship propellers," *International Shipbuilding Progress*, vol. 54, pp. 2–3, 2007.

[13] P. Koukouvinis, I. K. Karathanassis, and M. Gavaises, "Prediction of cavitation and induced erosion inside a high-pressure fuel pump," *International Journal of Engine Research*, vol. 19, no. 3, pp. 360–373, 2018. https://doi.org/10.1177/1468087417708137.

[14] M. Brunhart, C. Soteriou, C. Daveau, M. Gavaises, P. Koukouvinis, and M. Winterbourn, "Cavitation erosion risk indicators for a thin gap within a diesel fuel pump," *Wear*, p. 203024, 2019. https://doi.org/10.1016/j.wear.2019.203024.

[15] P. Koukouvinis, M. Gavaises, J. Li, and L. Wang, "Large eddy simulation of diesel injector including cavitation effects and correlation to erosion damage," *Fuel*, vol. 175, pp. 26 – 39, 2016. https://doi.org/10.1016/j.fuel.2016.02.037.

[16] M. Battistoni, D. Duke, A. B. Swantek, F. Z. Tilocco, C. F. Powell, and S. Som, "Effects of noncondensable gas on cavitating noxxles," *Atomization and Sprays*, vol. 25, no. 6, pp. 453–483, 2015. https://doi.org/10.1615/AtomizSpr.2015011076.

[17] M.-G. Mithun, P. Koukouvinis, I. K. Karathanassis, and M. Gavaises, "Numerical simulation of three-phase flow in an external gear pump using immersed boundary approach," *Applied Mathematical Modelling*, vol. 72, pp. 682 – 699, 2019. https://doi.org/10.1016/j.apm.2019.03.022.

[18] M. Tinguely, D. Obreschkow, P. Kobel, N. Dorsaz, A. de Bosset, and M. Farhat, "Energy partition at the collapse of spherical cavitation bubbles," *Phys. Rev. E*, vol. 86, p. 046315, 2012. https://doi.org/10.1103/PhysRevE.86.046315.

[19] T. Trummler, S. Schmidt, and N. Adams, "Large eddy simulation of a collapsing vapor bubble containing non-condensable gas," in *In Proceedings of 10th internationsal symposium on cavitation (CAV2018), Baltimore*, 2018. https://cav2018.jhu.edu/wp-content/uploads/Trummler-Theresa.pdf.

[20] T. Sato, M. Tinguely, M. Oizumi, and M. Farhat, "Evidence for hydrogen generation in laser- or spark-induced cavitation bubbles," *Applied Physics Letters*, vol. 102, no. 7, p. 074105, 2013. https://doi.org/10.1063/1.4793193.

[21] P. Koukouvinis, M. Gavaises, O. Supponen, and M. Farhat, "Numerical simulation of a collapsing bubble subject to gravity," *Physics of Fluids*, vol. 28, no. 3, p. 032110, 2016. https://doi.org/10.1063/1.4944561.

[22] P. Aleiferis, J. Serras-Pereira, A. Augoye, T. Davies, R. Cracknell, and D. Richardson, "Effect of fuel temperature on in-nozzle cavitation and spray formation of liquid hydrocarbons and alcohols from a real-size optical injector for direct-injection spark-ignition engines," *International Journal of Heat and Mass Transfer*, vol. 53, no. 21, pp. 4588–4606, 2010. https://doi.org/10.1016/j.ijheatmasstransfer.2010.06.033.

[23] D. Mamaikin, T. Knorsch, P. Rogler, P. Leick, and M. Wensing, "High speed shadowgraphy of transparent nozzles as an evaluation tool for in-nozzle cavitation behavior of gdi injectors," in *Conference: ILASS2017 - 28th European Conference on Liquid Atomization and Spray Systems*, 2017.

[24] S. Bornschlegel, C. Conrad, A. Durst, J. Wang, and M. Wensing, "Multi-hole gasoline direct injection:in-nozzle flow and primary breakup investigated in transparent nozzlesand with x-ray," *International Journal of Engine Research*, vol. 19, no. 1, pp. 67–77, 2018. `https://doi.org/10.1177/1468087417746860`.

[25] C. Conrad, S. Bornschlegel, A. Durst, D. Jordan, and M. Wensing, "Influence of the nozzle geometry on in-nozzle cavitation investigated in real-size glass nozzles with shadowgraphy and lif," in *ICLASS 2018, 14th Triennial International Conference on Liquid Atomization and Spray SystemsAt: Chicago, USA*, 2018.

[26] N. Mitroglou and M. Gavaises, "Cavitation inside real-size fully transparent fuel injector nozzles and its effect on near-nozzle spray formation," in *DIPSI workshop on droplet impact phenomena and spray investigations, University of Bergamo, Italy*, 2011.

[27] N. Mitroglou, V. Stamboliyski, I. Karathanassis, K. Nikas, and M. Gavaises, "Cloud cavitation vortex shedding inside an injector noz-

zle," *Experimental Thermal and Fluid Science*, vol. 84, pp. 179 – 189, 2017.

[28] I. K. Karathanassis, P. Koukouvinis, E. Kontolatis, Z. Lee, J. Wang, N. Mitroglou, and M. Gavaises, "High-speed visualization of vortical cavitation using synchrotron radiation," *Journal of Fluid Mechanics*, vol. 838, pp. 148–164, 2018. https://doi.org/10.1017/jfm.2017.885.

[29] E. Gomez Santos, J. Shi, M. Gavaises, C. Soteriou, M. Winterbourn, and W. Bauer, "Investigation of cavitation and air entrainment during pilot injection in real-size multi-hole diesel nozzles," *Fuel*, vol. 263, p. 116746, 2020.

[30] C. Arcoumanis, M. Gavaises, B. Argueyrolles, and F. Galzin, "Modeling of pressure-swirl atomizers for gdi engines," *SAE Transactions*, vol. 108, pp. 516–532, 1999.

[31] M. Gavaises, B. Reid, N. Mitroglou, G. Hargrave, C. Garner, E. Long, and R. Mcdavid, "On the formation of string cavitation inside fuel injectors," *Experiments in Fluids*, vol. 55, 2014. https://doi.org/10.1007/s00348-013-1662-8.

[32] N. Mitroglou, M. McLorn, M. Gavaises, C. Soteriou, and M. Winterbourne, "Instantaneous and ensemble average cavitation structures in

diesel micro-channel flow orifices," *Fuel*, vol. 116, pp. 736 – 742, 2014. https://doi.org/10.1016/j.fuel.2013.08.060.

[33] M.-C. Lai, F. Wang, X. Xie, J.-M. Shi, G. Dober, N. Guerrassi, Y. Meslem, Y. Gao, J. Wang, E. Durfresne, and S. Moon, "Correlating the nozzle flow to spray and primary breakup using visualization and multi-phase simulation," in *Conference: SIA Powertrain*, 2014.

[34] F. Orley, S. Hickel, S. J. Schmidt, and N. A. Adams, "Large-eddy simulation of turbulent, cavitating fuel flow inside a 9-hole diesel injector including needle movement," *International Journal of Engine Research*, vol. 18, no. 3, pp. 195–211, 2017. https://doi.org/10.1177/1468087416643901.

[35] M. Cristofaro, W. Edelbauer, P. Koukouvinis, and M. Gavaises, "Large Eddy Simulation of the Internal Injector Flow During Pilot Injection," in *Proceedings of the 10th International Symposium on Cavitation (CAV2018)*, ASME Press, 2018. https://doi.org/10.1115/1.861851_ch127.

[36] M. N. Theodorakakos A. and G. M, "Simulation of heating effects caused by extreme fuel pressurisation in cavitating flows through diesel fuel injectors," in *8th International Symposium on Cavitation, CAV2012, Singapore*, 2012.

[37] G. Strotos, P. Koukouvinis, A. Theodorakakos, M. Gavaises, L. Wang,

824 J. Li, and R. M. McDavid, "Fuel heating in high pressure diesel nozzles,"
825 in *THIESEL 2014 Conference on Thermo- and Fluid-Dynamic Processes*
826 *in Diesel Engines, Valencia, Spain*, 2014.

827 [38] A. Theodorakakos, G. Strotos, N. Mitroglou, C. Atkin, and M. Gavaises,
828 "Friction-induced heating in nozzle hole micro-channels under extreme
829 fuel pressurisation," *Fuel*, vol. 123, pp. 143 – 150, 2014. https://doi.
830 org/10.1016/j.fuel.2014.01.050.

831 [39] J. Shi, N. Guerrassi, G. Dober, K. Karimi, and Y. Meslem, "Complex
832 physics modelling of diesel injector nozzle flow and spray supported by
833 new experiments," in *Thiesel, Valencia*, 2014.

834 [40] G. Strotos, P. Koukouvinis, A. Theodorakakos, M. Gavaises, and
835 G. Bergeles, "Transient heating effects in high pressure diesel injector
836 nozzles," *International Journal of Heat and Fluid Flow*, vol. 51, pp. 257
837 – 267, 2015. https://doi.org/10.1016/j.ijheatfluidflow.2014.
838 10.010.

839 [41] R. Saurel and O. Lemetayer, "A multiphase model for compressible flows
840 with interfaces, shocks, detonation waves and cavitation," *Journal of*
841 *Fluid Mechanics*, vol. 431, pp. 239–271, 2001. https://doi.org/10.
842 1017/S0022112000003098.

843 [42] M. Cristofaro, W. Edelbauer, M. Gavaises, and P. Koukouvinis, "Nu-
844 merical simulation of compressible cavitating two-phase flows with a

pressure-based solver," in *Proceedings of the 28th Conference on Liquid Atomization and Spray Systems, ILASS Europe, Valencia*, 2017. http://dx.doi.org/10.4995/ILASS2017.2017.4629.

[43] M. Battistoni, S. Som, and D. Longman, "Comparison of mixture and multi-fluid models for in-nozzle cavitation prediction," in *Proceedings of ASME Internal Combustion Engine Division Fall Technical Conference, ICEF, Dearborn*, 2013.

[44] G. Schnerr and J. Sauer, "Physical and numerical modeling of unsteady cavitation dynamics," in *Proceedings. 4th International Conference on Multiphase Flow, ICMF-2001, New Orleans, USA*, 2001.

[45] P. J. Zwart, A. G. Gerber, and T. Belamri, "A two-phase flow model for predicting cavitation dynamics," in *Proceedings of the International Conference on Multiphase Flow, ICMF, Yokohama*, 2004.

[46] M. Kinzel, J. Lindau, and R. Kunz, "A unified homogenous multi-phase cfd model for cavitation," in *Proceedings of the ASME 2017 Fluids Engineering Division Summer Meeting (FEDSM2017), Waikoloa*, 2017. https://doi.org/10.1115/FEDSM2017-69363.

[47] P. Koukouvinis, H. Naseri, and M. Gavaises, "Performance of turbulence and cavitation models in prediction of incipient and developed cavitation," *International Journal of Engine Research*, vol. 18, no. 4, pp. 333–350, 2017. https://doi.org/10.1177/1468087416658604.

[48] E. Ghahramani and R. Bensow, "Analysis of the finite mass transfer models in the numerical simulation of bubbly flows," in *Proceedings of the 10th International Symposium on Cavitation (CAV2018)*, 2018. https://doi.org/10.1115/1.861851_ch18.

[49] S. Schenke, T. Melissaris, and T. J. C. van Terwisga, "On the relevance of kinematics for cavitation implosion loads," *Physics of Fluids*, vol. 31, no. 5, p. 052102, 2019. https://doi.org/10.1063/1.5092711.

[50] J. Shi and M. Arafin, "Cfd investigation of fuel property effect on cavitating flow in generic nozzle geometries," in *ILASS Europe 2010, 23rd Annual Conference on Liquid Atomization and Spray Systems, Brno, Czech Republic*, 2010.

[51] S. Washio, S. Fujiyoshi, and S. Takahashi, "Observation of cavitation inception in separating water flows through constricted channels," *Proceedings of the Institution of Mechanical Engineers, Part C: Journal of Mechanical Engineering Science*, vol. 223, no. 9, pp. 2071–2080, 2009. https://doi.org/10.1243/09544062JMES1438.

[52] S. J. Schmidt, M. Mihatsch, M. Thalhamer, and N. A. Adams, "Assessment of the prediction capability of a thermodynamic cavitation model for the collapse characteristics of a vapor-bubble cloud," in *In Proceedings of the WIMRC, 3rd International Cavitation Forum 2011, Warwick, UK*, 2011.

[53] C. P. Egerer, S. Hickel, S. J. Schmidt, and N. A. Adams, "Large-eddy simulation of turbulent cavitating flow in a micro channel," *Physics of Fluids*, vol. 26, no. 8, p. 085102, 2014. https://doi.org/10.1063/1.4891325.

[54] M. S. Mihatsch, *Numerical Prediction of Erosion and Degassing Effects in Cavitating Flows*. Dissertation, Technische Universitat Munchen, Munchen, 2017.

[55] C. Egerer, *Large-Eddy Simulation of Turbulent Cavitating Flows*. Dissertation, Technische Universitat Munchen, Munchen, 2016.

[56] P. Koukouvinis and M. Gavaises, "Simulation of throttle flow with two phase and single phase homogenous equilibrium model," *Journal of Physics: Conference Series*, vol. 656, p. 012086, 2015. https://doi.org/10.1088/1742-6596/656/1/012086.

[57] J.-L. Reboud, B. Stutz, and O. Coutier-Delgosha, "Two-phase flow structure of cavitation: experiment and modelling of unsteady effects.," in *Proceedings of the third international symposium on cavitation, Grenoble*, 1998.

[58] O. Coutier-Delgosha, J. L. Reboud, and Y. Delannoy, "Numerical simulation of the unsteady behaviour of cavitating flows," *International Journal for Numerical Methods in Fluids*, vol. 42, no. 5, pp. 527–548, 2003. https://doi.org/10.1002/fld.530.

[59] W. Edelbauer, J. Strucl, and A. Morozov, *Large Eddy Simulation of Cavitating Throttle Flow*, pp. 501–517. Singapore: Springer Singapore, 2016. https://doi.org/10.1007/978-981-287-615-7_34.

[60] A. Papoutsakis, A. Theodorakakos, E. Giannadakis, D. Papoulias, and M. Gavaises, "Les predictions of the vortical flow structures in diesel injector nozzles," *SAE Technical Papers*, no. 2009-01-0833, 2009.

[61] P. Koukouvinis, N. Mitroglou, M. Gavaises, M. Lorenzi, and M. Santini, "Quantitative predictions of cavitation presence and erosion-prone locations in a high-pressure cavitation test rig," *Journal of Fluid Mechanics*, vol. 819, pp. 21–57, 2017.

[62] E. Gomez Santos, J. Shi, W. Bauer, and M. Gavaises, "Modelling and prediction of cavitation erosion in gasoline direct injection injectors operated with e100 fuel using a barotropic equation of state," in *Proceedings of the IMechE Fuel Systems Conference, London*, 2018.

[63] R. Fortes Patella, A. Archer, and C. Flageul, "Numerical and experimental investigations on cavitation erosion," *IOP Conference Series: Earth and Environmental Science*, vol. 15, pp. 2013–, 2012. https://doi.org/10.1088/1755-1315/15/2/022013.

[64] T. Melissaris, N. Bulten, and T. Terwisga, "On cavitation aggressiveness and cavitation erosion on marine propellers using a urans

method," in *Proceedings of the 10th International Symposium on Cavitation (CAV2018)*, 2018. https://doi.org/10.1115/1.861851_ch160.

[65] C. Eskilsson and R. E. Bensow, "Estimation of cavitation erosion intensity using cfd: numerical compariosn of three different methods," in *In Proceedings of the Fourth International Symposium on Marine Propulsors, Austin, Texas, USA*, 2015. http://www.marinepropulsors.com/proceedings/2015/MA1-2.pdf last accessed 8th November 2019.

[66] D. Greif, A. Morozov, E. Winklhofer, and R. Tatschl, "Experimental and numerical investigation of erosive effects due to cavitation within injection equipment," in *Proceedings of 4th ICCHMT, Paris-Cachan, France, May 17-20*, 2005.

[67] G. M. Magnotti, M. Battistoni, K. Saha, and S. Som, "Influence of turbulence and thermophysical fluid properties on cavitation erosion predictions in channel flow geometries," *SAE Int. J. Adv. & Curr. Prac. in Mobility*, vol. 1, pp. 691–705, 2019.

[68] K. Saha, S. Som, M. Battistoni, Y. Li, E. Pomraning, and P. K. Senecal, "Numerical investigation of two-phase flow evolution of in- and near-nozzle regions of a gasoline direct injection engine during needle transients," *SAE Int. J. Engines*, vol. 9, pp. 1230–1240, 2016.

[69] E. Baldwin, R. Grover, S. Parrish, D. Duke, K. Matusik, C. Powell, A. Kastengren, and D. Schmidt, "String flash-boiling in gaso-

line direct injection simulations with transient needle motion," *International Journal of Multiphase Flow*, vol. 87, pp. 90 – 101, 2016. https://doi.org/10.1016/j.ijmultiphaseflow.2016.09.004.

[70] Z. Yue, M. Battistoni, and S. Som, "Spray characterization for engine combustion network spray g injector using high-fidelity simulation with detailed injector geometry," *International Journal of Engine Research*, vol. 21, no. 1, pp. 226–238, 2020. https://doi.org/10.1177/1468087419872398.

[71] *Data from NIST Standard Reference Database 69: NIST Chemistry WebBook*. https://webbook.nist.gov/cgi/cbook.cgi?ID=C64175&Mask=4&Type=ANTOINE&Plot=on#Refs last accessed 12th November 2019.

[72] *ANSYS Fluent User Manual*, 2018.

[73] B. Vreman, B. Geurts, and H. Kuerten, "Subgrid-modelling in les of compressible flow," *Applied Scientific Research*, vol. 54, no. 3, pp. 191–203, 1995.

[74] B. Vreman, B. Geurts, and H. Kuerten, "Large-eddy simulation of the turbulent mixing layer," *Journal of Fluid Mechanics*, vol. 339, p. 357â390, 1997.

[75] E. Garnier, N. Adams, and P. Sagaut, *Large Eddy Simulation for Compressible Flows*. Springer, 2009.

[76] F. Nicoud and F. Ducros, "Subgrid-scale stress modelling based on the square of the velocity gradient tensor," *Flow, Turbulence and Combustion*, vol. 62, no. 3, pp. 183–200, 1999. https://doi.org/10.1023/A:1009995426001.

[77] S. B. Pope, *Turbulent Flows*. Cambridge University Press, 2000.

[78] F. R. Menter, "Two-equation eddy-viscosity turbulence models for engineering applications," *AIAA Journal*, vol. 32, no. 8, pp. 1598–1605, 1994. https://doi.org/10.2514/3.12149.

[79] C. Song, J. He, F. Zhou, and G. Wang, "Numerical simulation of cavitating and non-cavitating flows over a hydrofoil," *Report prepared for the office of Naval Research U.S. Navy, Department of Defense*, p. 83, 04 1997.

[80] G. Watson, C. K. Zeberg-Mikkelsen, A. Baylaucq, and C. Boned, "High-pressure density measurements for the binary system ethanol + heptane," *J. Chem. Eng. Data*, vol. 51, no. 1, pp. 112–118, 2006. https://doi.org/10.1021/je050261u.

[81] J. Shi, P. Aguado Lopez, G. Dober, N. Guerrassi, W. Bauer, and M. Lai, "Using les and x-ray imaging to understand the influence of injection hole geometry on diesel spray formation," in *Thiesel, Valencia*, 2016.

[82] J. Shi, P. Aguado Lopez, E. Gomez Santos, N. Guerrassi, G. Dober, W. Bauer, M. Lai, and J. Wang, "Evidence of vortex driven primary

breakup in high pressure fuel injection," in *Proceedings of the 28th Conference on Liquid Atomization and Spray Systems, ILASS Europe, Valencia*, 2017. http://dx.doi.org/10.4995/ILASS2017.2017.5707.

[83] J. Shi, P. Aguado Lopez, N. Guerrassi, and G. Dober, "Understanding high-pressure injection primary breakup by using large eddy simulation and x-ray spray imaging," *MTZ worldwide*, vol. 78, pp. 50–57, 2017. https://doi.org/10.1007/s38313-017-0039-4.

[84] J. Shi, P. Aguado Lopez, E. Gomez Santos, N. Guerrasi, W. Bauer, M.-C. Lai, and J. Wang, "High pressure diesel spray development: the effect of nozzle geometry and flow vortex dynamics," in *Proceedings of the 14th International Conference on Liquid Atomization and Spray Systems, ICLASS, Chicago*, 2018.

[85] J. Shi, E. Gomez Santos, G. Hoffmann, and G. Dober, "Large eddy simulation as an effective tool for gdi nozzle development," *MTZ worldwide*, vol. 79, pp. 58–63, 2018. https://doi.org/10.1007/s38313-018-0089-2.

[86] H. Tennekes and J. Lumley, *A First Course in Turbulence*. MIT Press, 1972.

[87] K. Yasutomi, J. Hwang, J. Manin, L. Pickett, M. Arienti, S. Daly, and S. Skeen, "Diesel injector elasticity effects on internal nozzle flow," in

2019 JSAE/SAE Powertrains, Fuels and Lubricants, SAE International, 2019.

[88] Z. Chen and A. Przekwas, "A coupled pressure-based computational method for incompressible/compressible flows," *Journal of Computational Physics*, vol. 229, no. 24, pp. 9150 – 9165, 2010. https://doi.org/10.1016/j.jcp.2010.08.029.

[89] J. Ferziger and M. Peric, *Computational Methods for Fluid Dynamics*. Springer Berlin Heidelberg, 2012.

[90] B. Leonard, "The ultimate conservative difference scheme applied to unsteady one-dimensional advection," *Computer Methods in Applied Mechanics and Engineering*, vol. 88, no. 1, pp. 17 – 74, 1991. https://doi.org/10.1016/0045-7825(91)90232-U.

[91] F. R. Menter, "Best practice: scale-resolving simulations in ansys cfd," in *ANSYS Technical report*, 2015.

[92] M. Cristofaro, W. Edelbauer, P. Koukouvinis, and M. Gavaises, "A numerical study on the effect of cavitation erosion in a diesel injector," *Applied Mathematical Modelling*, vol. 78, pp. 200 – 216, 2020. https://doi.org/10.1016/j.apm.2019.09.002.

[93] S. Schenke and T. J. van Terwisga, "An energy conservative method to predict the erosive aggressiveness of collapsing cavitating structures and cavitating flows from numerical simulations," *International Journal of*

Multiphase Flow, vol. 111, pp. 200 – 218, 2019. https://doi.org/10.1016/j.ijmultiphaseflow.2018.11.016.

[94] A. Vogel and W. Lauterborn, "Acoustic transient generation by laser produced cavitation bubbles near solid boundaries," *The Journal of the Acoustical Society of America*, vol. 84, no. 2, pp. 719–731, 1988. https://doi.org/10.1121/1.396852.

[95] M. S. Mihatsch, S. J. Schmidt, and N. A. Adams, "Cavitation erosion prediction based on analysis of flow dynamics and impact load spectra," *Physics of Fluids*, vol. 27, no. 10, p. 103302, 2015.

[96] S. Schenke and T. Terwisga, "Simulating compressibility in cavitating flows with an incompressible mass transfer flow solver," in *In Proceedings of the 5th International Symposium on Marine Propulsion (SMP 2017) at: Espoo, Finland*, 2017.

[97] M. Gavaises, D. Papoulias, A. Andriotis, E. Giannadakis, and A. Theodorakakos, "Link between cavitation development and erosion damage in diesel injector nozzles," in *SAE World Congress & Exhibition*, SAE International, 2007. https://doi.org/10.4271/2007-01-0246.

[98] M. Gold, R. Pearson, J. Turner, D. Sykes, V. Stetsyuk, G. de Sercey, C. Crua, F. Koukouvinis, and M. Gavaises, "Simulation and measurement of transient fluid phenomena within diesel injection," *SAE*

1052 *Int. J. Adv. & Curr. Prac. in Mobility*, vol. 1, pp. 291–305, 2019.
1053 https://doi.org/10.4271/2019-01-0066.